Emergence of irreversible decoherence from unitary dynamics

Ri-Hua Zheng,¹ Jia-Hao Lü,¹ Fan Wu,¹ Yan Xia,^{1,*} Li-Hua Lin,^{1,2} Zhen-Biao Yang,^{1,2,†} and Shi-Biao Zheng^{1,2,‡}

¹ Fujian Key Laboratory of Quantum Information and Quantum Optics,

College of Physics and Information Engineering, Fuzhou University, Fuzhou, Fujian, 350108, China

² Hefei National Laboratory, Hefei 230088, China

The decoherence of superpositions of classically distinguishable states (cat states) is crucial for understanding quantum-to-classical transitions and quantum measurements. So far, decoherence processes of mesoscopic cat states have been demonstrated in several experiments. However, the issue of how the unitary system-reservoir dynamics can lead to irreversible system decoherence remains largely unexplored in experiments. Here we experimentally explore this fundamental issue with a circuit quantum electrodynamics device, where a bus microwave resonator storing a photonic cat state is connected to many nonlinear electronic oscillators. Each of these oscillators that are effectively coupled to the bus resonator serves as one degree of freedom of the reservoir. By gradually increasing the number of the reservoir's degrees of freedom, we find that the revivable quantum coherence progressively decays, owing to the growth in the amount of inerasable information about the system's state encoded in the reservoir. Our results illustrate that irreversible decoherence of a quantum system is an emergent phenomenon, arising from the unitary dynamics involving the system and many of the reservoir's degrees of freedom, which is crucial for the reconciliation of quantum mechanics and classical physics.

The superposition principle lies at the heart of quantum mechanics and discriminates between the microscopic and macroscopic worlds [1, 2]. It allows a quantum system to be simultaneously in two states corresponding to different values of an observable, whose quantum interference gives rise to new effects that cannot be interpreted in classical terms. The validity of this principle has passed a large number of experimental tests and lays the foundation for quantum technology, ranging from quantum information transmission and processing [3] to quantum metrology [4–6]. Despite these huge successes, it remains a mystery as to why such quantum superpositions cannot appear in macroscopic, everyday objects. For example, we have never observed a biological system that suspends between the alive and dead states, as illustrated in the famous Schrödinger cat paradox [7].

The solution to this issue is central to understanding the quantum measurement process, during which the meter turns one of the suspending choices into a classical reality by correlating its state with that of the quantum system to be monitored [8]. It has been argued that the environment is responsible for the final emergence of such a classical reality [2]. Any quantum system would unavoidably couple to its surrounding environment, which corresponds to a reservoir that involves many degrees of freedom. A zero-temperature reservoir can be thought of as an ensemble of electromagnetic modes, each of which is initially in its ground state. The coupling between the system and reservoir results in their entanglement. In terms of complementarity, the environment continuously gathers which-path information about the system [9–14], destroying the quantum coherence between the superimposed states (paths), thereby transforming their quantum superposition into a classical mixture. This process is referred to as decoherence, which happens at a rate that scales linearly with the size of the quantum superposition.

The quantum coherence for a macroscopic meter is lost too fast to observe. However, a mesoscopic superposition of states, which is distinguished by some classical property, offers the possibility for exploring the decoherence process and the quantum-to-classical transition [15, 16]. Such mesoscopic cat states are usually defined as superpositions of coherent states with distinct amplitudes or phases of a bosonic mode. In addition to fundamental interest, such superposition states are useful for fault-tolerant quantum computation [17, 18] and quantum metrology [19–23]. Over the past three decades, enduring efforts have been devoted to experimental investigations of irreversible decoherence processes of these mesoscopic superpositions in different systems, including photonic fields [8, 15, 24], motional modes of trapped ions [25–27], and mechanical oscillators [28]. These experiments provide a deep insight into the elusive quantum-to-classical transition, but do not reveal how the irreversible decoherence emerges from the unitary system-reservoir interaction dynamics. In 1997, Raimond, Brune, and Haroche described a reversible decoherence process [29], where the cavity containing a photonic cat state is coupled to a second cavity, which serves as a non-Markovian "single-mode reservoir". Under this system-reservoir interaction, the mesoscopic quantum coherence would exhibit periodic collapses and revivals due to the fact that the which-path information encoded in the reservoir mode can be erased by the later interaction. It was argued that when more and more "reservoir modes" are involved, the standard irreversible decoherence model is recovered. This approach, highlighting the connection between decoherence and complementarity, provides an illuminating interpretation for usual irreversible decoherence, but experimental demonstrations remain elusive.

Here we perform an in-depth investigation on the reversible-to-irreversible transition of decoherence in both theory and experiment. We focus on the evolution of a system field mode in a reservoir consisting of nonlinear oscillators, each corresponding to a qubit. The reservoir acquires the which-path information of the system by energy exchange, which is reversible for the single-qubit case. Such a process becomes more chaotic with the increase of the number

of the reservoir qubits, since different qubits exchange energy with the field mode at different rates. Consequently, the which-path information acquired by the reservoir cannot be erased when the reservoir contains sufficiently many qubits. We demonstrate such a controlled decoherence process with a circuit quantum electrodynamics (QED) architecture, where a bus resonator, initially prepared in a quantum superposition of being empty and filled with a coherent field, is controllably coupled to an engineered reservoir composed of Josephsonjunction-based nonlinear oscillators. We extract the whichpath information encoded in the reservoir from the measured output density matrices of the qubits. With the increase of the number of reservoir qubits, the amount of inerasable whichpath information diminishes, and the revivable quantum coherence of the photonic cat state reduces. The experimental results demonstrate that the irreversible decoherence phenomenon can emerge from a unitary system-environment interaction, by which the system's which-path information is irreversibly distributed among a large number of the reservoir's degrees of freedom.

The system under investigation is a bosonic field mode, which is coupled to a reservoir involving N nonlinear oscillators. Each of these reservoir oscillators is confined within its lowest two levels, and thus corresponds to a qubit. In the framework rotating at the system frequency, the system-reservoir interaction is described by the Hamiltonian

$$H = \sum_{k=1}^{N} \left[\delta_k \left| e \right\rangle_k \left\langle e \right| + \frac{\lambda_k}{2} \left(a \left| e \right\rangle_k \left\langle g \right| + a^{\dagger} \left| g \right\rangle_k \left\langle e \right| \right) \right], \quad (1)$$

where a^\dagger and a represent the creation and annihilation operators for the system field mode, and $|e\rangle_k$ and $|g\rangle_k$ denote the upper and lower levels for the kth qubit, which interacts with the system with the strength $\lambda_k/2$ and detuning δ_k . We first consider the case that the reservoir involves only a single qubit and the field mode is initially in a coherent state $|\alpha\rangle$, which represents a quantum state with a close classical analog and can be expanded in terms of photon-number states

$$|\alpha\rangle = e^{-|\alpha|^2/2} \sum_{n=0}^{\infty} \frac{\alpha^n}{\sqrt{n!}} |n\rangle.$$
 (2)

Suppose that the average photon number, $\langle n \rangle = |\alpha|^2$, is much larger than the width of the Poissonian photon-number distribution $|\alpha|$. The qubit, initially in the ground state $|g\rangle_1$, undergoes Rabi oscillations with the period $2\pi/\Omega_1$, where $\Omega_1 = \sqrt{\langle n \rangle (\lambda_1)^2 + (\delta_1)^2}$ is the Rabi frequency. During the interaction, the qubit produces a backaction on the coherent field by splitting it into two components rotating at the angular velocities $\pm \omega_1 = \pm \lambda_1^2/(4\Omega_1)$ [30, 31]. When the time t is much smaller than π/ω , this backaction can be neglected, so that the field mode approximately remains in the quasiclassical state $|\alpha\rangle$.

We now turn to the decoherence process of an amplitude photonic cat state during interaction with a single-qubit reservoir. Such a cat state is formed by the superposition of a coherent state and the vacuum state,

$$|\mathcal{C}\rangle \simeq (|0\rangle + |\alpha\rangle)/\sqrt{2}.$$
 (3)

As the qubit is initially in its ground state, it is decoupled from the field's vacuum component $|0\rangle$. Under the above condition, the conditional Rabi dynamics evolves the qubit and the resonator into an entangled state, approximated by $[|0\rangle\,|g\rangle_1 + |\alpha\rangle\,(c_1^g\,|g\rangle_1 + c_1^e\,|e\rangle_1)]/\sqrt{2}$, where $c_1^g = \cos\theta + i\delta_1\sin\theta/\Omega_1$ and $c_1^e = -i\sqrt{\langle n\rangle}\lambda_1\sin\theta/\Omega_1$ with $\theta = \Omega_1 t/2$. This entanglement partially encodes the information about the field amplitude in the qubit state, which results in the degradation of quantum coherence between $|0\rangle$ and $|\alpha\rangle$. When the qubit is traced out, the field is left in a mixed state, described by the density operator

$$\rho_c = [|0\rangle\langle 0| + |\alpha\rangle\langle \alpha| + c_1^g(|0\rangle\langle \alpha| + |\alpha\rangle\langle 0|)]/2.$$
 (4)

Consequently, the coherence is reduced by a factor of $\eta=|c_1^g|$. As the which-path information about the photonic cat state encoded in the qubit can be erased by the later field-qubit interaction, the decoherence process is reversible.

The amount of the revivable coherence would become less and less when the number of qubits in the reservoir is increased. When the field mode is coupled to a bath involving N qubits, each initially in its ground state, the total system-reservoir state approximately evolves as

$$|\psi(t)\rangle \simeq (|0\rangle |\phi^{|0\rangle}\rangle + |\alpha\rangle |\phi^{|\alpha\rangle}\rangle)/\sqrt{2},$$
 (5)

where $|\phi^{\text{\tiny{IO}}}\rangle=\bigotimes_{k=1}^N|g\rangle_k$ and $|\phi^{\text{\tiny{IO}}}\rangle=\bigotimes_{k=1}^N(c_k^g|g\rangle_k+c_k^e|e\rangle_k)$. The result is valid when the number of photons leaked to the reservoir, $\sum_{k=1}^N|c_k^e|^2$, is much smaller than $|\alpha|^2$. When all degrees of freedom of the reservoir are traced out, the field's density operator reduces to

$$\rho_c = \frac{1}{2} \left[|0\rangle\langle 0| + |\alpha\rangle\langle \alpha| + \left(\prod_{k=1}^N c_k^g |\alpha\rangle\langle 0| + \text{H.c.} \right) \right]. \quad (6)$$

If the reservoir contains many qubits that have different Rabi frequencies, the phases of their Rabi oscillations cannot be resynchronized so that the which-path information encoded in the collective state of the qubits cannot be erased, leading to an irreversible decoherence process.

The model is realized in a circuit QED architecture, where 10 frequency-tunable Josephson-junction-based nonlinear oscillators are capacitively coupled to a bus resonator (B) with a fixed frequency $\omega_s/(2\pi)=5.796$ GHz, as sketched in Fig. 1(a) [32, 33]. The photonic mode stored in B corresponds to the system field mode. Two of these nonlinear oscillators, denoted as A_1 and A_2 , are respectively used as ancillas for preparing the cat state and for detecting the quantum coherence of the system field mode stored in B, while the others serve as the reservoir oscillators, represented by Q_j (j=1 to 8). The on-resonance coupling strengths between these nonlinear oscillators and B range from $2\pi \times 13$ to $2\pi \times 21$ MHz.

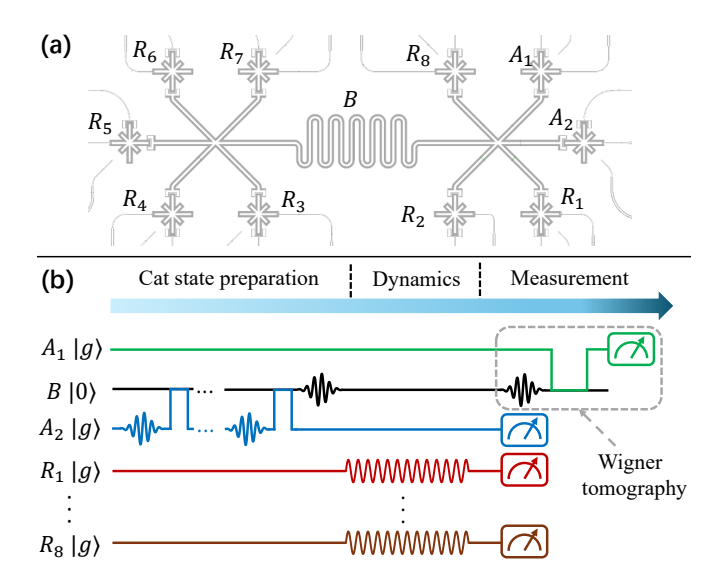


FIG. 1. (a) Sketch of the device. The circuit quantum electrodynamics architecture contains a frequency-fixed bus resonator (B) connected to 10 frequency-tunable Josephson-junction-based nonlinear oscillators, each of which is confined to the lowest two levels and behaves as a qubit. Two of these qubits, denoted as A_1 and A_2 , are used as ancillas to prepare the photonic cat state of the photonic mode stored in B and to probe its quantum coherence, respectively. The other qubits, labeled $Q_1 - Q_8$, serve as the reservoir oscillators that can be selectively coupled to B.

Each nonlinear oscillator has an anharmonicity $\sim 2\pi \times 250$ MHz, which enables it to behave well as a qubit. Before the experiment, each of the qubits stays at its idle frequency, where it is effectively decoupled from the system resonator as the detuning is much larger than the corresponding coupling strength. The system parameters are detailed in Sec. S1 of Supplementary Material [34]. The experiment starts with the preparation of the cat state, following the step-bystep technique proposed in the context of cavity OED [35], and demonstrated in ion trap [36] and circuit QED experiments [37, 38]. To shorten the pulse sequence, we first drive the resonator from the initial ground state to the phase cat state $(|-\alpha/2\rangle + |\alpha/2\rangle)/\sqrt{2}$ using A_1 , initially in its ground state, which coherently pumps photons from an external microwave source into B one by one, thanks to the tunability of the frequency of A_1 , enabled by an ac flux. The size of the cat state is characterized by the parameter α , which has a value of 3.3 in our experiment.

We first consider the decoherence behavior of the photonic cat state coupled to a single reservoir qubit (Q_1) . Figure 1(b) shows the pulse sequence for realizing this reversible decoherence process and probing the quantum coherence after this process. We first transform the phase cat state into the desired amplitude cat state by the phase-space displacement $D(\alpha/2)$. Then Q_1 is effectively coupled to B by applying an ac flux, which parametrically modulates the qubit angular frequency as $\omega_1 = \omega_s - \nu_1 + \varepsilon_1 \cos(\nu_1 t) + \delta_1$, where ε_1 and ν_1 are the modulation amplitude and frequency, respectively. When

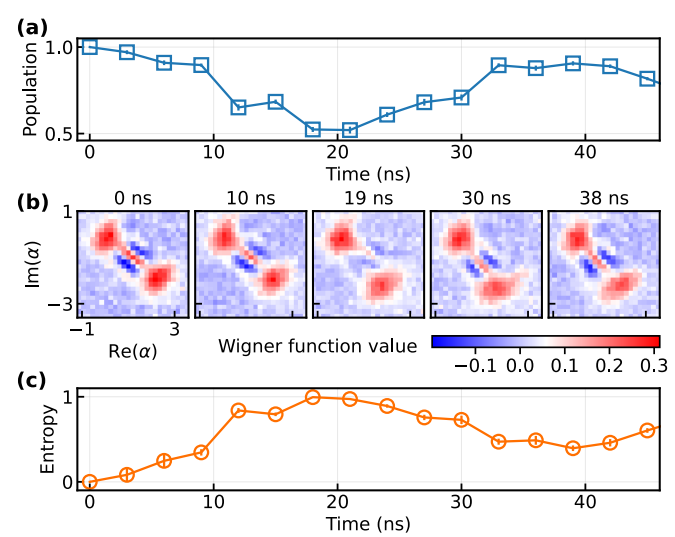


FIG. 2. Observation of the reversible decoherence of the cat state induced by a single reservoir qubit (Q_1) . (a) The $|g\rangle$ -state population of Q_1 measured for different interaction times t. (b) Wigner functions of the mesoscopic field for different B- Q_1 interaction times. (c) Evolution of the von Neumann entropy of Q_1 . Before the interaction, B is prepared in the amplitude cat state of Eq. (3) with $\alpha=3.3$ and Q_1 is initialized in its ground state $|g\rangle_1$.

 $\delta_1\ll\nu_1$, this qubit interacts with the resonator at the first upper sideband with respect to the modulation, with and effective coupling strength $\lambda_1/2=J_1(\mu_1)\xi_1$ [39–41], where ξ_1 is the on-resonance $B\text{-}Q_1$ photon swapping rate and $J_1(\mu_1)$ represents the first-order Bessel function of the first kind, with $\mu_1=\varepsilon_1/\nu_1$. The resulting $B\text{-}Q_1$ interaction is described by the effective Hamiltonian of Eq. (1) with N=1. In our experiment, λ_1 and δ_1 are set to $2\pi\times8.1$ and 0 MHz, respectively. After a preset interaction time, the modulation is switched off. The $|g\rangle$ -state population of Q_1 , P_g , measured for different interaction times t, is displayed in Fig. 2(a). As expected, this population shows an oscillatory pattern with the period T=38 ns.

To illustrate the resulting decoherence process of the mesoscopic field, we perform Wigner tomography with the assistance of A_2 . The Wigner function of the field describes the phase-space quasi-probability distribution. The value of this function at position β , denoted as $\mathcal{W}(\beta)$, is equal to the expectation value of the photon number parity after the phase-space displacement $D(-\beta) = e^{-\beta a^{\dagger} + \beta^* a}$. The photon-number distribution of the displaced field state is inferred by the Rabi signals of A_2 resonantly coupled to the resonator. The Wigner functions, reconstructed for different B- Q_1 interaction times, are displayed in Fig. 2(b). The quantum coherence of the initial cat state is manifested by the interference fringes with alternating positive and negative values between the two Gaussian peaks, each corresponding to one quasi-classical state component. At time t = 19 ns, the two field components $|0\rangle$ and $|\alpha\rangle$ are respectively correlated with the two orthogonal qubit states $|g\rangle_1$ and $|e\rangle_1$, so that quantum coherence is

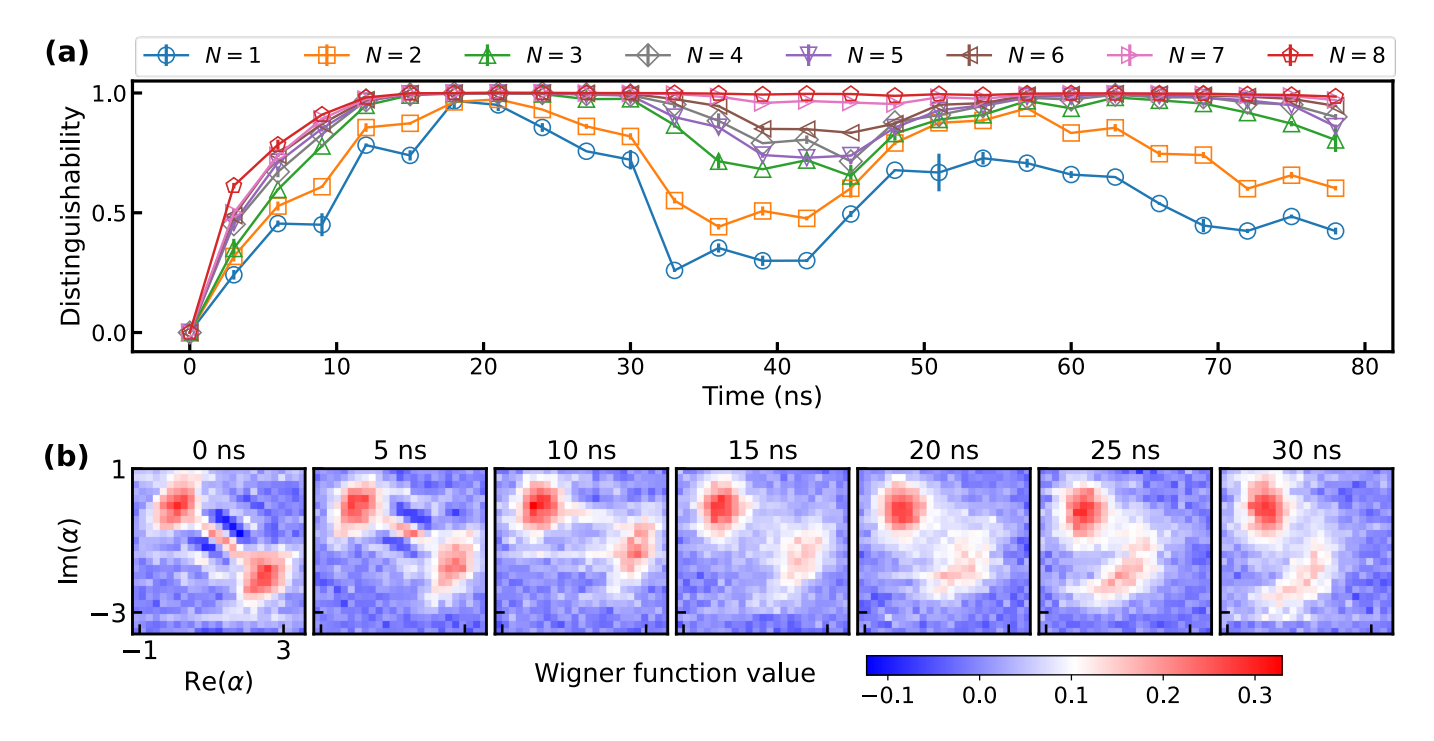


FIG. 3. Progressive transition from reversible to irreversible decoherence. (a) Evolutions of distinguishabilities for different values of N. A total of N (N=1 to 8) reservoir oscillators are selectively coupled to the system, prepared in the amplitude cat state. The effective coupling strength and detuning associated with each qubit are controlled by the parameters of the modulation pulses applied to mediate the corresponding sideband interactions. (b) Wigner functions of the mesoscopic field for N=8, measured for different interaction times.

completely lost when the qubit state is traced out. At time $t=38\,\mathrm{ns}$, the field is disentangled with the qubit which makes a full cycle of Rabi oscillations for the field component $|\alpha\rangle$, and consequently, the quantum coherence is revived. In terms of complementarity, the qubit can be considered as a which-path detector in phase space. The path information is encoded in the qubit's state and then erased by the unitary dynamics, leading to disappearance and revival of the phase-space interference.

The B- Q_1 entanglement can be characterized by the von Neumann entropy of the output state of Q_1 , defined as $\mathcal{S} = -\mathrm{Tr}(\rho_q\log_2\rho_q)$, where ρ_q denotes the reduced density matrix of Q_1 . Figure 2(c) presents the entropy measured for different B- Q_1 interaction times. As expected, the entropy exhibits an oscillatory pattern. During the first stage, \mathcal{S} quickly increases, reaching the maximum at time t=19 ns when B and Q_1 evolve to a maximally entangled state. Then \mathcal{S} drops and returns to the minimum value at time t=38 ns.

The transition from reversible to irreversible decoherence is illustrated by gradually increasing the number of qubits (N) that are effectively coupled to the bus resonator. To make the coherent state $|\alpha\rangle$ well remain quasi-classical during the interaction, we suitably set the effective strengths and detunings of the sideband interactions so that the total number of photons transferred from $|\alpha\rangle$ to the qubits is negligible compared with $|\alpha|^2$. The frequencies and amplitudes of the modulations, used to mediate sideband interactions between the bus resonator and reservoir oscillators, are detailed in Sec. S4 of

Supplementary Material [34].

It is convenient to quantify the loss of the quantum coherence of the mesoscopic field in terms of the which-path information stored in the reservoir with the distinguishability \mathcal{D} [10], defined as

$$\mathcal{D} = \frac{1}{2} \text{Tr} \left| \rho^{|0\rangle} - \rho^{|\alpha\rangle} \right|, \tag{7}$$

where $\rho^{|0\rangle}$ and $\rho^{|\alpha\rangle}$ respectively denote the reduced density operators for the reservoir qubits associated with the field components $|0\rangle$ and $|\alpha\rangle$ after the system-reservoir interaction. The value of \mathcal{D} ranges from 0 to 1, depending upon the amount of the which-path information that can be extracted from the reservoir in principle. For $\rho^{|0\rangle} = \rho^{|\alpha\rangle}$, $\mathcal{D} = 0$. In this case, the reservoir contains no information about whether the field mode is in $|0\rangle$ or $|\alpha\rangle$, so that the quantum coherence keeps intact. When $\rho^{|0\rangle}$ and $\rho^{|\alpha\rangle}$ are orthogonal, $\mathcal{D} = 1$, which corresponds to the case that the reservoir contains unambiguous information about the amplitude of the field mode, destroying the system's quantum coherence. As each reservoir qubit remains in the ground state $|g\rangle_k$ for the vacuum field state $|0\rangle$, we have $\rho^{|0\rangle} = \bigotimes_{k=1}^N |g\rangle_k \langle g|$. The output density matrix of the kth reservoir qubit (ρ_k) for the cat state is the equal mixture of $|g\rangle_k \langle g|$ and $\rho_k^{|\alpha\rangle}$, where $\rho_k^{|\alpha\rangle}$ is the output state of this qubit associated with $|\alpha\rangle$. Therefore, $\rho_k^{|\alpha\rangle}$ can be inferred from the measured ρ_k : $\rho_k^{|\alpha\rangle} = 2\rho_k - |g\rangle_k \langle g|$ and $\rho^{|\alpha\rangle}$ is given by $\rho^{|\alpha\rangle} = \bigotimes_{k=1}^N \rho_k^{|\alpha\rangle}$.

Figure 3(a) shows the evolutions of the distinguishabilities for different values of N, inferred from the individually measured output states of the reservoir oscillators. As expected, for N=1, \mathcal{D} exhibits an oscillatory pattern. When N is increased, the oscillatory pattern is gradually washed out. For N=8, \mathcal{D} almost remains unchanged after it reaches the maximum at time t=16 ns. These results can be interpreted as follows. The transition $|g\rangle \rightarrow |e\rangle$ for a single reservoir qubit associated with $|\alpha\rangle$ is sufficient to determine which quasiclassical component the field mode is in. As the Rabi oscillations of different reservoir qubits are non-synchronous, the probability for all qubits to return to their ground states decreases when N is increased. Consequently, with the increase of N, the which-path information acquisition process becomes more and more irreversible.

To further confirm that the distinguishability is closely related to the quantum coherence between the two quasiclassical components $|0\rangle$ and $|\alpha\rangle$ of the field mode, we observe the evolution of the output field state for N=8. The Wigner functions of the field mode, measured for different interaction times with the reservoir, are displayed in Fig. 3(b). As expected, the interference fringes between the two Gaussian peaks are gradually washed out during the interaction, without revival. This coincides with the evolution of \mathcal{D} , which also exhibits irreversible behavior for this case.

In conclusion, we have investigated the decoherence process of a photonic cat state coupled to an artificial reservoir formed by nonlinear oscillators. By coupling the photonic mode to more and more reservoir oscillators, we observe the progressive reversible-to-irreversible transition of the decoherence process of the mesoscopic field. Our results reveal that the amount of the revivable quantum coherence between the two superimposed quasiclassical components of the system depends upon the amount of the erasable which-path information encoded in the reservoir. When the number of the reservoir oscillators is sufficiently large, this information, once acquired by the reservoir, cannot be erased during the later interaction due to the non-synchronization of the quantum oscillations associated with distinct reservoir oscillators. Consequently, the observed phase-space quantum interference effect irreversibly decays. The experiment implies that the irreversible quantum decoherence is an emergent phenomenon arising from the unitary dynamics involving the quantum system and the reservoir, shedding new light on the physics underlying the behavior of open quantum systems.

This work was supported by the National Natural Science Foundation of China (Grant Nos. 12274080, 12474356, 12475015, and 62471143), the Key Program of the National Natural Science Foundation of Fujian Province (Grant No. 2024J02008), and the Innovation Program for Quantum Science and Technology (Grant No. 2021ZD0300200).

- † zbyang@fzu.edu.cn
- t96034@fzu.edu.cn
- [1] W. H. Zurek, Decoherence and the transition from quantum to classical, Phys. Today 44, 36 (1991).
- [2] W. H. Zurek, Decoherence, einselection, and the quantum origins of the classical, Rev. Mod. Phys. 75, 715 (2003).
- [3] M. A. Nielsen and I. L. Chuang, Quantum Computation and Quantum Information (Cambridge Univ. Press, 2000).
- [4] C. L. Degen, F. Reinhard, and P. Cappellaro, Quantum sensing, Rev. Mod. Phys. 89, 035002 (2017).
- [5] K. C. McCormick, J. Keller, S. C. Burd, D. J. Wineland, A. C. Wilson, and D. Leibfried, Quantum-enhanced sensing of a mechanical oscillator, Nature 572, 86 (2019).
- [6] W. Wang, Y. Wu, Y. Ma, W. Cai, C. Lu, X. Xu, X. Mu, Y. Xu, Z.-J. Chen, H. Wang, Y. P. Song, H. Yuan, C.-L. Zou, L.-M. Duan, and L. Sun, Heisenberg-limited single-mode quantum metrology, Nat. Commun. 10, 4382 (2019).
- [7] E. Schrödinger, Die gegenwärtige situation in der quantenmechanik, Naturwissenschaften 23, 807 (1935).
- [8] M. Brune, E. Hagley, J. Dreyer, X. Maître, A. Maali, C. Wunderlich, J. M. Raimond, and S. Haroche, Observing the progressive decoherence of the "meter" in a quantum measurement, Phys. Rev. Lett. 77, 4887 (1996).
- [9] M. O. Scully, B.-G. Englert, and H. Walther, Quantum optical tests of complementarity, Nature 351, 111 (1991).
- [10] B.-G. Englert, Fringe visibility and which-way information: An inequality, Phys. Rev. Lett. 77, 2154 (1996).
- [11] E. Buks, R. Schuster, M. Heiblum, D. Mahalu, and V. Umansky, Dephasing in electron interference by a "which-path" detector, Nature 391, 871 (1998).
- [12] S. Dürr, T. Nonn, and G. Rempe, Fringe visibility and whichway information in an atom interferometer, Phys. Rev. Lett. 81, 5705 (1998).
- [13] P. Bertet, S. Osnaghi, A. Rauschenbeutel, G. Nogues, A. Auffeves, M. Brune, J. M. Raimond, and S. Haroche, A complementarity experiment with an interferometer at the quantum-classical boundary, Nature 411, 166 (2001).
- [14] X.-J. Huang, P.-R. Han, N. Wen, S.-B. Yang, X. Zhu, J.-H. Lü, R.-H. Zheng, H. Li, Z.-B. Yang, K. Xu, C.-P. Yang, Q.-C. Wu, D. Zheng, H. Fan, and S.-B. Zheng, Entanglement-interference complementarity and experimental demonstration in a superconducting circuit, npj Quantum Inf. 9, 43 (2023).
- [15] S. Haroche, Nobel lecture: Controlling photons in a box and exploring the quantum to classical boundary, Rev. Mod. Phys. 85, 1083 (2013).
- [16] D. J. Wineland, Nobel lecture: Superposition, entanglement, and raising Schrödinger's cat, Rev. Mod. Phys. 85, 1103 (2013).
- [17] N. Ofek, A. Petrenko, R. Heeres, P. Reinhold, Z. Leghtas, Y. Vlastakis, Y. Liu, L. Frunzio, S. M. Girvin, L. Jiang, M. Mirrahimi, M. H. Devoret, and R. J. Schoelkopf, Extending the lifetime of a quantum bit with error correction in superconducting circuits, Nature 536, 441 (2016).
- [18] A. Grimm, N. E. Frattini, S. Puri, S. Mundhada, S. Touzard, M. Mirrahimi, S. M. Girvin, S. Shankar, and M. H. Devoret, Stabilization and operation of a Kerr-cat qubit, Nature 584, 205 (2020).
- [19] F. Toscano, D. A. R. Dalvit, L. Davidovich, and W. H. Zurek, Sub-planck phase-space structures and Heisenberglimited measurements, Phys. Rev. A 73, 023803 (2006).
- 20] M. Penasa, S. Gerlich, T. Rybarczyk, B. Meillón, M. Brune, J. M. Raimond, S. Haroche, L. Davidovich, and I. Dotsenko, Measurement of a microwave field amplitude beyond the standard quantum limit, Phys. Rev. A 94, 022313 (2016).

^{*} xia-208@163.com

- [21] B. Vlastakis, G. Kirchmair, Z. Leghtas, S. E. Nigg, L. Frunzio, S. M. Girvin, M. Mirrahimi, M. H. Devoret, and R. J. Schoelkopf, Deterministically encoding quantum information using 100-photon Schrödinger cat states, Science 342, 607 (2013).
- [22] X. Tan, T. Krisnanda, A. Duina, K. Park, C. Y. Song, C. Fontaine, A. Copetudo, R. Filip, Y. Yu, and Y. Gao, Realization of versatile and effective quantum metrology using a single bosonic mode, PRX Quantum 6, 010304 (2025).
- [23] X.-W. Zheng, J.-C. Zheng, X.-F. Zheng, P. Pan, and P. Li, Quantum-enhanced sensing of bosonic modes with cat states, Phys. Rev. A 112, 032612 (2025).
- [24] S. Deléglise, I. Dotsenko, C. Sayrin, J. Bernu, M. Brune, J.-M. Raimond, and S. Haroche, Reconstruction of non-classical cavity field states with snapshots of their decoherence, Nature 455, 510 (2008).
- [25] C. J. Myatt, B. E. King, Q. A. Turchette, C. A. Sackett, D. Kielpinski, W. M. Itano, C. Monroe, and D. J. Wineland, Decoherence of quantum superpositions through coupling to engineered reservoirs, Nature 403, 269 (2000).
- [26] Q. A. Turchette, C. J. Myatt, B. E. King, C. A. Sackett, D. Kielpinski, W. M. Itano, C. Monroe, and D. J. Wineland, Decoherence and decay of motional quantum states of a trapped atom coupled to engineered reservoirs, Phys. Rev. A 62, 053807 (2000).
- [27] C. J. Myatt, B. E. King, Q. A. Turchette, C. A. Sackett, D. Kielpinski, W. M. Itano, C. Monroe, and D. J. Wineland, Decoherence of motional states of trapped ions, J. Mod. Opt. 47, 2181 (2000).
- [28] M. Bild, M. Fadel, Y. Yang, U. von Lüpke, P. Martin, A. Bruno, and Y. Chu, Schrödinger cat states of a 16-microgram mechanical oscillator, Science 380, 274 (2023).
- [29] J. M. Raimond, M. Brune, and S. Haroche, Reversible decoherence of a mesoscopic superposition of field states, Phys. Rev. Lett. 79, 1964 (1997).
- [30] A. Auffèves, P. Maioli, S. Meunier, S. Gleyzes, G. Nogues, M. Brune, J. M. Raimond, and S. Haroche, Entanglement of a mesoscopic field with an atom induced by photon graininess in a cavity, Phys. Rev. Lett. 91, 230405 (2003).
- [31] S.-B. Zheng, R.-X. Zheng, and Q. Chen, Entanglement transfer between atomic qubits and thermal fields, Quantum Inf. Comput. **13**, 531 (2013).
- [32] C. Song, K. Xu, W. Liu, C.-P. Yang, S.-B. Zheng, H. Deng, Q. Xie, K. Huang, Q. Guo, P. Zhang, D. Zhang, D. Xu, X. Zheng, X. Zhu, H. Wang, Y.-A. Chen, C.-Y. Lu, S. Han, and J.-W. Pan, 10-qubit entanglement and parallel logic operations

- with a superconducting circuit, Phys. Rev. Lett. **119**, 180511 (2017).
- [33] R.-H. Zheng, N. Wen, J.-H. Jiao, X.-J. Yu, W. Fan, C.-L. Deng, Z.-B. Yang, K. Zeng, D. Xu, D. Zheng, H. Fan, and S.-B. Zheng, Experimental demonstration of spontaneous symmetry breaking with emergent multi-qubit entanglement, Phys. Rev. Lett. 134, 150046 (2025).
- [34] See the Supplemental Material, which includes Refs. [35, 37, 41], for the description of qubit and resonator parameters, preparation of initial cat states in the resonator, calibration of qubit Z-line signals, realization of sideband coupling via Floquet modulation, measurement of photon-number distribution and Wigner tomography, and the derivation and calculation of distinguishability.
- [35] C. K. Law and J. H. Eberly, Arbitrary control of a quantum electromagnetic field, Phys. Rev. Lett. 76, 1055 (1996).
- [36] A. Ben-Kish, B. DeMarco, V. Meyer, M. Rowe, J. W. Britton, W. M. Itano, B. Jelenković, C. Langer, D. Leibfried, T. Rosenband, and D. J. Wineland, Experimental demonstration of a technique to generate arbitrary quantum superposition states of a harmonically bound spin-1/2 particle, Phys. Rev. Lett. 90, 037902 (2003).
- [37] M. Hofheinz, H. Wang, M. Ansmann, R. C. Bialczak, E. Lucero, M. Neeley, A. D. O'Connell, D. Sank, J. Wenner, J. M. Martinis, and A. N. Cleland, Synthesizing arbitrary quantum states in a superconducting resonator, Nature 459, 546 (2009).
- [38] S.-B. Zheng, Y.-P. Zhong, K. Xu, J.-J. Qu, H. Wang, L. Wang, C.-P. Shen, J. M. Yang, J. M. Martinis, A. N. Cleland, S.-Y. Shen, and C.-P. Yang, Quantum delayed-choice experiment with a beam splitter in a quantum superposition, Phys. Rev. Lett. 115, 260403 (2015).
- [39] X. Li, J. Yu, T. Han, Y. Chen, W. Xu, H. Cai, Y. P. Wang, Z.-Y. Song, Z.-Q. Xue, L. Yin, and L. Sun, Perfect quantum state transfer in a superconducting qubit chain with parametrically tunable couplings, Phys. Rev. Appl. 10, 054009 (2018).
- [40] D.-W. Wang, C. Song, W. Feng, H. Cai, D. Xu, H. Deng, H. Li, D. Zheng, X. Zhu, H. Wang, S.-Y. Zhu, and M. O. Scully, Synthesis of antisymmetric spin-exchange interaction and chiral spin clusters in superconducting circuits, Nat. Phys. 15, 382 (2019).
- [41] R.-H. Zheng, N. Wen, N. Ye, Y.-H. Chen, J.-H. Liu, L.-T. Li, K. Shen, Y.-R. Xu, D. Zhang, X. Du, Y. Li, F. Xia, Z.-B. Wu, A. Yang, A. Miranowicz, N. Lambert, P. Fan, F. Nori, B. Zheng, and S.-B. Zheng, Observation of a superradiant phase transition with emergent cat states, Phys. Rev. Lett. 131, 113601 (2023).

Supplemental Material for "Emergence of irreversible decoherence from unitary dynamics"

Ri-Hua Zheng,¹ Jia-Hao Lü,¹ Fan Wu,¹ Yan Xia,^{1,*}
Li-Hua Lin,^{1,2} Zhen-Biao Yang,^{1,2,†} and Shi-Biao Zheng^{1,2,‡}

¹Fujian Key Laboratory of Quantum Information and Quantum Optics,

College of Physics and Information Engineering,

Fuzhou University, Fuzhou, Fujian, 350108, China

²Hefei National Laboratory, Hefei 230088, China

CONTENTS

S1. Qubit and Resonator Parameters	2
S2. Preparation of Initial Cat States in the Resonator	3
A. Phase-cat preparation via sequential photon-number swaps	3
B. From a phase cat to an amplitude cat via cavity displacement	nt 5
S3. Calibration of Qubit Z-Line Signals	8
A. Mapping Z-line Square Pulse Amplitude to Qubit Frequence	y 8
B. Verification of Z-Pulse Square-Wave Integrity	9
C. Calibration of Qubit Z-Line Crosstalk	10
S4. Sideband Coupling via Floquet Modulation	13
A. Experimental demonstration of sideband coupling	14
S5. Photon Number Distribution Measurement and Wigner Tomog	raphy 16
A. Photon-number readout via a resonant ancilla qubit	16
B. Wigner tomography	17
S6. Derivation and Calculation of Distinguishability	18
A. Definition	18
B. Distinguishability and many-qubit reservoir	19
C. Ensuring Positive Semidefinite Reconstruction	20
References	20

Parameters	R_1	R_2	R_3	R_4	R_5	R_6	R_7	R_8	A_1	A_2
$\omega_i/(2\pi)$ (GHz)	5.30	5.25	5.15	5.35	4.95	5.05	5.00	5.12	5.20	5.10
F_g	0.95	0.97	0.95	0.93	0.92	0.95	0.94	0.93	0.95	0.94
F_e	0.89	0.88	0.86	0.85	0.79	0.87	0.87	0.88	0.81	0.87
$\omega_r/(2\pi)$ (GHz)	6.695	6.697	6.638	6.617	6.619	6.544	6.511	6.892	6.811	6.792
$\omega_h/(2\pi)$ (GHz)	5.775	5.777	5.714	5.723	5.728	5.746	5.748	5.786	5.923	5.822
T_1 (μ s)	14.9	29.8	15.6	14.4	13.1	24.7	26.8	15.5	25.5	14.0
$T_2 (\mu s)$	3.0	2.4	2.6	3.2	1.6	2.0	2.1	2.2	2.5	2.0
$T_2^{ m SE}\left(\mu{ m s} ight)$	11.7	10.1	10.0	10.3	8.5	10.2	8.6	8.6	9.3	8.0
ξ (2 π MHz)	19.6	19.9	16.0	20.2	19.2	20.5	12.9	16.3	19.8	19.0

TABLE S1. **Performance of superconducting qubits.** The table lists ten qubits $(R_1-R_8 \text{ and } A_1-A_2)$. The entry $\omega_i/(2\pi)$ denotes the idle frequency used as the reference for state preparation and standby operation. Frequency tuning is implemented through the Z control line by applying direct-current offsets together with square-wave bias pulses, which shift the qubit frequency; the highest reached frequency is $\omega_h/(2\pi)$. Readout fidelities are F_g and F_e . Coherence parameters T_1 , T_2 , and $T_2^{\rm SE}$ are measured at each qubit's idle frequency, with T_1 representing energy relaxation, T_2 obtained from Ramsey dephasing (Gaussian fit), and $T_2^{\rm SE}$ from spin-echo (exponential fit). Each qubit is read out through a dedicated resonator of frequency $\omega_r/(2\pi)$ and couples to the common bus (storage) resonator with strength ξ .

S1. QUBIT AND RESONATOR PARAMETERS

The device comprises ten superconducting qubits, labeled R_1 – R_8 and A_1 – A_2 , whose performance metrics are summarized in Table S1. Qubit operation is referenced to the idle point $\omega_i/(2\pi)$: this is the frequency where qubit states are prepared and where a qubit resides whenever it is not involved in dynamical protocols. Frequency excursions are realized via the Z control line, which allows fast tuning of the qubit frequency; the highest accessible point reached in this way is denoted $\omega_h/(2\pi)$. Coherence metrics are characterized at the idle point, with T_1 quantifying energy relaxation, T_2 obtained from Ramsey interferometry, and $T_2^{\rm SE}$ extracted with spin–echo. State discrimination is evaluated by F_g and F_e . Each qubit is dispersively coupled to its dedicated readout resonator of frequency $\omega_r/(2\pi)$, and couples to the common bus resonator (serving as the storage mode) with strength ξ .

For the bus (storage) resonator, the fixed frequency is $\omega_s/(2\pi)=5.796$ GHz, with an energy-relaxation time of $T_{1,s}=3.0~\mu s$ and a dephasing time of $T_{2,s}=3.8~\mu s$. Both $T_{1,s}$ and $T_{2,s}$ are extracted by resonantly tuning a qubit into the cavity and swapping the cavity excitations to the qubit. The relaxation of the mapped excitation yields $T_{1,s}$, while Ramsey measurement on the qubit after the swap provide $T_{2,s}$.

S2. PREPARATION OF INITIAL CAT STATES IN THE RESONATOR

A. Phase-cat preparation via sequential photon-number swaps

We target the even cat

$$|C_{+}(\alpha/2)\rangle = \mathcal{N}_{+}(|\alpha/2\rangle + |-\alpha/2\rangle), \qquad \mathcal{N}_{+} = \left[2(1 + e^{-|\alpha|^{2}/2})\right]^{-1/2},$$
 (S1)

whose Fock decomposition contains only even photon numbers,

$$|C_{+}(\alpha/2)\rangle = \sum_{m=0}^{\infty} c_{2m} |2m\rangle, \qquad c_{2m} = \mathcal{N}_{+} \frac{2(\alpha/2)^{2m}}{\sqrt{(2m)!}} e^{-|\alpha|^{2}/8}.$$
 (S2)

Since only even components are present and the coefficients c_{2m} decrease rapidly with m, we work in a truncated resonator subspace. For the cat size used here $(\alpha/2 = 1.65)$, more than 98.9% of the probability lies in $n \leq 6$. We therefore fix an operational cutoff $N^* = 6$ and design the time-reversed sequence to explicitly empty the n-excitation manifolds $\operatorname{span}\{|g,n\rangle,|e,n-1\rangle\}$ for $n=6,5,\ldots,1$; components with n>6 are left untouched and contribute only a negligible tail to the final fidelity.

On each n-excitation manifold, a resonant swap S_n (under the Jaynes–Cummings interaction) of duration t_n performs

$$\begin{pmatrix} a'_{g,n} \\ a'_{e,n-1} \end{pmatrix} = \begin{pmatrix} \cos \theta_n & -i \sin \theta_n \\ -i \sin \theta_n & \cos \theta_n \end{pmatrix} \begin{pmatrix} a_{g,n} \\ a_{e,n-1} \end{pmatrix}, \qquad \theta_n = \sqrt{n} \, \xi \, t_n, \tag{S3}$$

where ξ denotes the qubit–resonator coupling strength. A single-qubit rotation Q_n within $\{|g, n-1\rangle, |e, n-1\rangle\}$ is taken as

$$Q_n = X_\pi = \exp\left(-i\frac{\pi}{2}\sigma_x\right),\tag{S4}$$

and no additional phase gate is employed.

Backward selection rule. Starting from the exact target $|\Psi_{\text{tar}}\rangle = |g\rangle \otimes |C_{+}(\alpha/2)\rangle$, at each n choose θ_n so that the amplitude on $|g,n\rangle$ is removed by S_n :

$$\theta_n = \frac{\pi}{2} + \arctan\left(\frac{a_{e,n-1}}{ia_{g,n}}\right), \qquad \Rightarrow \qquad a'_{g,n} = 0.$$
 (S5)

Then apply a fixed single-qubit flip $Q_n = X_\pi = \exp(-i\frac{\pi}{2}\sigma_x)$ within $\{|g,n-1\rangle, |e,n-1\rangle\}$ to transfer the residual population to $|g,n-1\rangle$ [S1]. Applying Eqs. (S3)–(S5) for $n=6,5,\ldots,1$ gives a six-step backward sequence; the forward (experimental) order is the reverse:

$$Q_1 \rightarrow S_1 \rightarrow Q_2 \rightarrow S_2 \rightarrow \cdots \rightarrow Q_6 \rightarrow S_6, \qquad t_n = \frac{\theta_n}{\sqrt{n}\,\xi}.$$
 (S6)

Fidelity of the truncated cat state. To quantify the error introduced by fixing the cutoff at $N^* = 6$, we evaluate the overlap between the ideal even cat and its projection onto the truncated Fock subspace for the experimental parameter $\alpha = 3.3$. The state used as input to the backward construction is

$$|\psi_6\rangle = |g\rangle \otimes \frac{\Pi_{\leq 6}|C_+(\alpha/2)\rangle}{\sqrt{\text{Tr}[\Pi_{\leq 6}|C_+(\alpha/2)\rangle]}}, \qquad \Pi_{\leq 6} = \sum_{n=0}^6 |n\rangle\langle n|.$$
 (S7)

For $\alpha/2 = 1.65$, the nonvanishing (even) Fock amplitudes are

$$c_0 \simeq 0.36, \qquad c_2 \simeq 0.70, \qquad c_4 \simeq 0.55, \qquad c_6 \simeq 0.27.$$
 (S8)

The intrinsic fidelity set by the truncation is therefore

$$F = \left| \langle \psi_6 | C_+(\alpha/2) \rangle \right|^2 = \sum_{n \in \{0, 2, 4, 6\}} |c_n|^2 \simeq 0.989, \tag{S9}$$

so the neglected probability weight above n=6 is about 1.07%. This fixes the truncation-limited baseline. Table S2 A compiles the six-step backward sequence (the time-reverse of the laboratory protocol for $\alpha/2=1.65$), listing the chosen angles θ_n and the resulting system state after each operation; when read from top to bottom, it traces the population flow toward the vacuum, whereas the forward preparation is executed in the opposite order.

By construction of the angles in Table S2 A, the backward-elimination rule ensures that applying the sequence in the order $Q_1S_1\cdots Q_6S_6$ to the target state recovers the vacuum:

$$Q_1 S_1 \cdots Q_6 S_6 |\psi_6\rangle = |\psi_0\rangle. \tag{S10}$$

Taking the adjoint and reversing the order gives the ideal preparation from vacuum to the target,

$$|\psi_6\rangle = S_6^{\dagger} Q_6^{\dagger} \cdots S_1^{\dagger} Q_1^{\dagger} |\psi_0\rangle. \tag{S11}$$

For experimental convenience (to avoid excessively long or short swap durations on each n-manifold), we implement instead the laboratory "forward" composition

$$U_{\text{fwd}} = S_6 Q_6 \cdots S_1 Q_1, \qquad |\psi_{\text{fwd}}\rangle = U_{\text{fwd}} |\psi_0\rangle.$$
 (S12)

We now show that this forward implementation also prepares $|\psi_6\rangle$.

Each elementary step acts on the two-dimensional subspace $\{|g\rangle\otimes|n\rangle, |e\rangle\otimes|n-1\rangle\}$. In this manifold,

$$S_n(\theta_n) = \exp(-i\theta_n \sigma_x), \qquad Q_n = X_\pi = \exp\left(-i\frac{\pi}{2}\sigma_x\right) = -i\sigma_x.$$
 (S13)

Introduce the block-diagonal operator $Z = \bigoplus_n Z_n$ with

$$Z_n = |g\rangle\langle g| \otimes |n\rangle\langle n| - |e\rangle\langle e| \otimes |n-1\rangle\langle n-1|, \qquad Z_n\sigma_x Z_n = -\sigma_x.$$
 (S14)

Hence

$$Z_n S_n(\theta_n) Z_n = S_n^{\dagger}(\theta_n), \qquad Z_n Q_n Z_n = Q_n^{\dagger}.$$
 (S15)

Using Eq. (S15) repeatedly and $Z^2 = \mathbb{I}$, we obtain

$$S_6^{\dagger} Q_6^{\dagger} \cdots S_1^{\dagger} Q_1^{\dagger} = Z \left(S_6 Q_6 \cdots S_1 Q_1 \right) Z = Z U_{\text{fwd}} Z. \tag{S16}$$

Since both endpoints lie in the ground-qubit sector, $Z|\psi_0\rangle=|\psi_0\rangle$ and $Z|\psi_6\rangle=|\psi_6\rangle$. Using $S_6^\dagger Q_6^\dagger \cdots S_1^\dagger Q_1^\dagger=Z\,U_{\rm fwd}\,Z$ then gives

$$|\psi_6\rangle = Z U_{\text{fwd}} Z |\psi_0\rangle = U_{\text{fwd}} |\psi_0\rangle.$$
 (S17)

Thus the forward composition prepares the target exactly. Any sign differences induced by Z affect only intermediate $|e\rangle\otimes|n-1\rangle$ components and are absent at the endpoints.

Figure S1(a) visualizes the evolution in the forward direction: panels from top to bottom correspond to steps 1–6 of the laboratory sequence and show how population is redistributed among the n-excitation manifolds as the protocol proceeds. For comparison, Fig. S1(b) shows the Wigner function of the ideal even cat $|C_{+}(\alpha/2)\rangle$ with $\alpha/2=1.65$, while Fig. S1(c) presents the Wigner function computed from the theoretical state $|\psi_6\rangle$ produced by the forward sequence, whose close agreement confirms the effectiveness of the protocol.

B. From a phase cat to an amplitude cat via cavity displacement

Building on the six-step protocol and its backward verification in Fig. S1, we next convert the prepared phase cat $|C_{+}(\alpha/2)\rangle$ into a standard amplitude cat by a calibrated cavity displacement.

The state in Fig. S2(a) is the even phase cat

$$|C_{+}(\alpha/2)\rangle = \mathcal{N}_{+}(|\alpha/2\rangle + |-\alpha/2\rangle),$$
 (S18)

where \mathcal{N}_+ is the normalization factor. To obtain an amplitude cat of the form $|0\rangle + |\alpha\rangle$, we apply the displacement operator

$$D(\beta) = \exp(\beta a^{\dagger} - \beta^* a), \qquad D(\beta) |\gamma\rangle = e^{i\operatorname{Im}(\beta\gamma^*)} |\gamma + \beta\rangle.$$
 (S19)

Choosing $\beta = \alpha/2$ gives,

$$D(\alpha/2) |C_{+}(\alpha/2)\rangle = \mathcal{N}_{+} (|\alpha\rangle + |0\rangle). \tag{S20}$$

Sequence of states,	Operational	System state			
operations	parameter				
$ \psi_6\rangle$		$ g\rangle\otimes \left(0.36 0\rangle + 0.70 2\rangle + 0.55 4\rangle + 0.27 6\rangle\right)$			
S_6	$\theta_6 = 1.57$				
Q_6	X_{π}				
1.1.		$ g\rangle\otimes(-0.55 1\rangle-0.52 3\rangle-0.27 5\rangle)$			
$ \psi_5 angle$		$-i e\rangle\otimes (0.36 0\rangle + 0.43 2\rangle + 0.16 4\rangle)$			
S_5	$\theta_5 = 2.09$				
Q_5	X_{π}				
$ \psi_4 angle$		$ g\rangle\otimes \left(0.23 0\rangle+0.54 2\rangle+0.31 4\rangle\right)$			
		$+i e angle\otimes(0.62 1 angle+0.40 3 angle)$			
S_4	$\theta_4 = 2.48$				
Q_4	X_{π}				
$ \psi_3 angle$		$ g angle\otimes(-0.65 1 angle-0.51 3 angle)$			
Ψ3/		$-i e angle\otimes (0.23 0 angle + 0.51 2 angle)$			
S_3	$\theta_3 = 2.35$				
Q_3	X_{π}				
$ \psi_2\rangle$		$ g\rangle\otimes(0.59 0\rangle+0.72 2\rangle)+i e\rangle\otimes(0.36 1\rangle)$			
S_2	$\theta_2 = 2.03$				
Q_2	X_{π}				
$ \psi_1\rangle$		$ g angle\otimes(-0.80 1 angle)-i e angle\otimes(0.59 0 angle)$			
S_1	$\theta_1 = 2.20$				
Q_1	X_{π}				
$ \psi_0 angle$		$ g angle\otimes 0 angle$			

TABLE S2. Six-step backward sequence for $\alpha/2 = 1.65$. Entries list the swap angle θ_n (for S_n) and the resulting system state after each operation. Rows are given in backward order; the laboratory implementation applies them from bottom to top (forward order).

Experimentally, $D(\beta)$ is realized by a short resonant microwave pulse applied on the cavity with drive Hamiltonian

$$H_d(t) = \hbar \left(\epsilon a^{\dagger} e^{-i\omega_s t} + \epsilon^* a e^{i\omega_s t} \right), \tag{S21}$$

where $\omega_s/(2\pi)$ denotes the cavity frequency. In the cavity frame rotating at ω_s , this reduces to $\tilde{H}_d(t)=\hbar(\epsilon a^\dagger+\epsilon^*a)$ and produces a net displacement

$$U(t) = \mathcal{T} \exp\left[-\frac{i}{\hbar} \int_0^t \tilde{H}_d(\tau) d\tau\right] = D(\beta), \qquad \beta = -i \int_0^t \epsilon(\tau) d\tau.$$
 (S22)

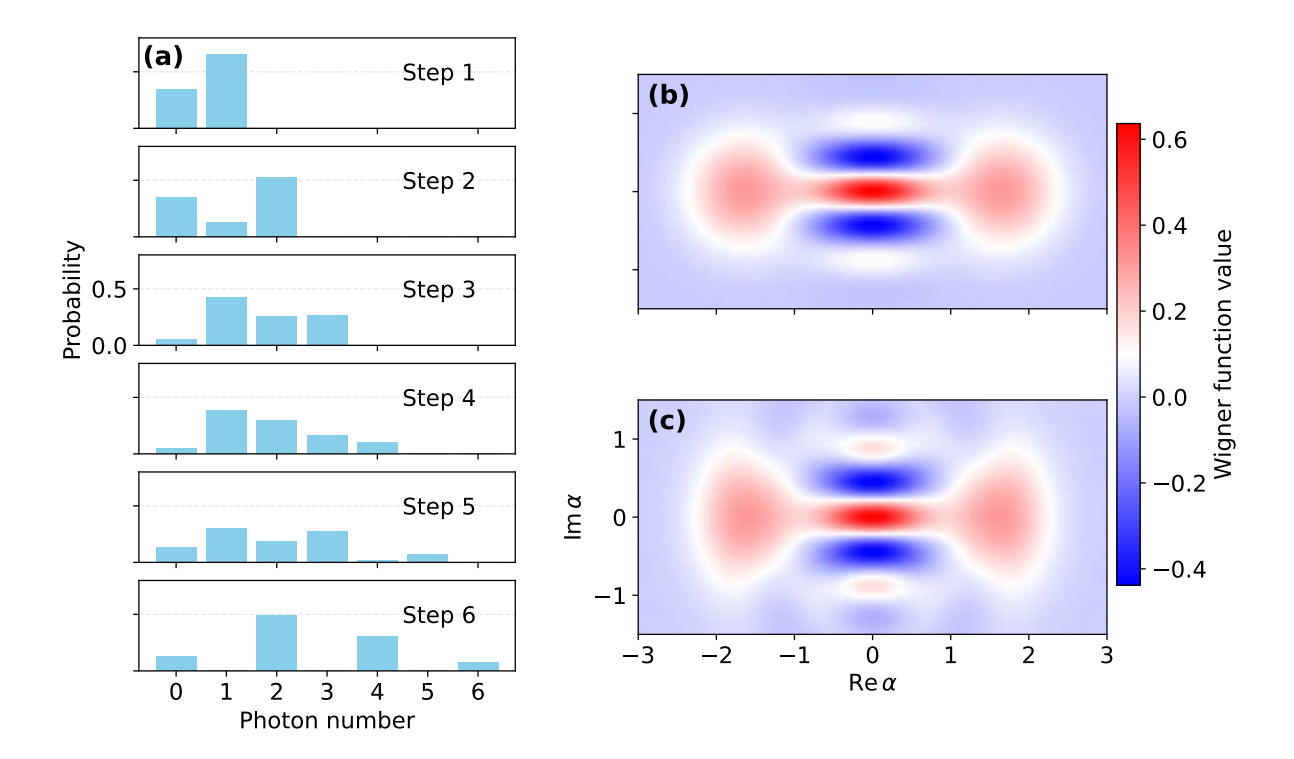


FIG. S1. Forward six-step protocol. (a) Photon-number distributions (n=0-6) for the intermediate resonator states obtained by the six-step protocol in Table S2 A; panels from top to bottom correspond to the forward steps 1–6, showing how population is progressively transferred from lower to higher n-excitation manifolds. Reversing the tabulated operations gives the backward sequence used for analysis. (b) Wigner function of the ideal even cat $|C_{+}(\alpha/2)\rangle$ with $\alpha/2=1.65$ ($\alpha=3.3$). (c) Wigner function computed from the theoretical state $|\psi_6\rangle$ produced by the forward sequence. The color bar indicates the Wigner-function value; axes are labeled by Re α and Im α .

By setting $|\beta| = |\alpha|/2$ and aligning $\arg \beta$ along the real axis, the phase cat $|C_+(\alpha/2)\rangle$ is translated into the amplitude cat $\mathcal{N}_+(|0\rangle + |\alpha\rangle)$.

In Fig. S2 we display the Wigner functions of the prepared phase and amplitude cats. For clarity, these plots are shown after a small de-rotation applied to the measured states, since in practice the experimentally measured Wigner functions can appear rotated in phase space. This rotation originates from a mismatch between the AC-Stark shifts accumulated in the experimental rotating frame and those in the tomography rotating frame, which can be modeled as an additional effective term $\hbar\delta\chi\,a^{\dagger}a$. The accumulated difference $\theta=\int \delta\chi\,dt$ implements a phase-space rotation $R(\theta)=e^{-i\theta a^{\dagger}a}$. We de-rotate the measured states before plotting, so that the Wigner functions displayed in Fig. S2 correspond to the intended cat states rather than their rotated versions.

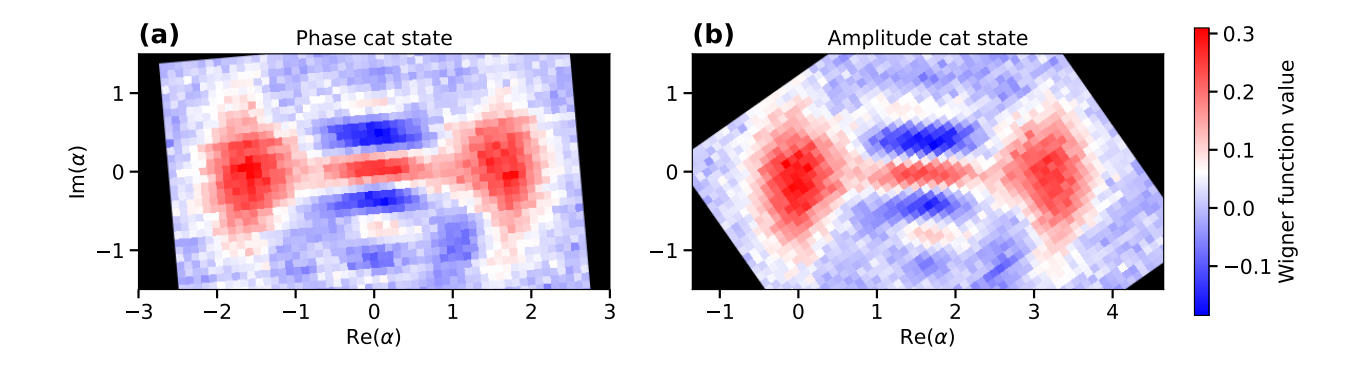


FIG. S2. Displacing a phase cat to an amplitude cat. (a) Wigner tomography of the phase cat prepared by the photon-by-photon protocol, $\mathcal{N}_+(|\alpha/2\rangle+|-\alpha/2\rangle)$. (b) After a resonant displacement $D(\alpha/2)$, the coherent components move to 0 and α , yielding the amplitude cat $\mathcal{N}_+(|0\rangle+|\alpha\rangle)$. Small phase-space rotations arise because the AC-Stark shifts in the experimental rotating frame and in the tomography rotating frame are not identical, producing a net angle ϑ described by $R(\vartheta)=e^{-i\vartheta a^\dagger a}$. All Wigner plots are de-rotated for clarity.

S3. CALIBRATION OF QUBIT Z-LINE SIGNALS

Before turning to the specific calibration routines, we note that the purpose of characterizing qubit Z-line signals is to ensure that subsequent Floquet-type modulations are both accurate and reproducible. Because sideband coupling via Floquet modulation relies on precise periodic driving through the Z lines, any static miscalibration of Z-line amplitudes, waveform distortions, or inter-qubit crosstalk would directly degrade the modulation accuracy. Therefore, in this section we establish a set of calibrations for the Z-line signals of all qubits, including amplitude-to-frequency mapping, verification of square-wave integrity, and compensation of Z-line crosstalk. These steps guarantee that the Z-line drive serves as a reliable and calibrated control channel for the Floquet protocols introduced later.

A. Mapping Z-line Square Pulse Amplitude to Qubit Frequency

In this calibration, we determine the function $f_q(\mathrm{ZPA})$ that maps the Z-line square-pulse amplitude (ZPA) to the qubit frequency. The Z line is driven by a square wave whose flat-top amplitude sets the qubit frequency, while a microwave tone on the XY line is used as a spectroscopy probe. The pulse sequence used for this procedure is illustrated in Fig. S3(a): initialize the qubit in $|g\rangle$, then apply a concurrent XY microwave tone and a Z-line square wave, followed by a projective measurement. We present qubit R_7 as a representative example; the same protocol is applied to all other qubits to obtain their individual $f_q^{(i)}(\mathrm{ZPA})$.

For a fixed ZPA, we sweep the XY-drive frequency concurrently with the Z-line square wave and record the excited-state population. The resonance peak gives the qubit frequency at that ZPA. Repeating this over a range of ZPAs yields the two-dimensional map shown in Fig. S3(b) (excited-state population $P_{|e\rangle}$ versus XY-drive frequency and ZPA). The bright ridge traces $f_q(\text{ZPA})$, which we extract by fitting the ridge with a polynomial fit. The resulting calibration is then used for precise frequency placement via Z-line control in subsequent experiments. The same mapping-and-fit workflow is performed for each remaining qubit to build a per-qubit lookup table and to update it as needed prior to data acquisition.

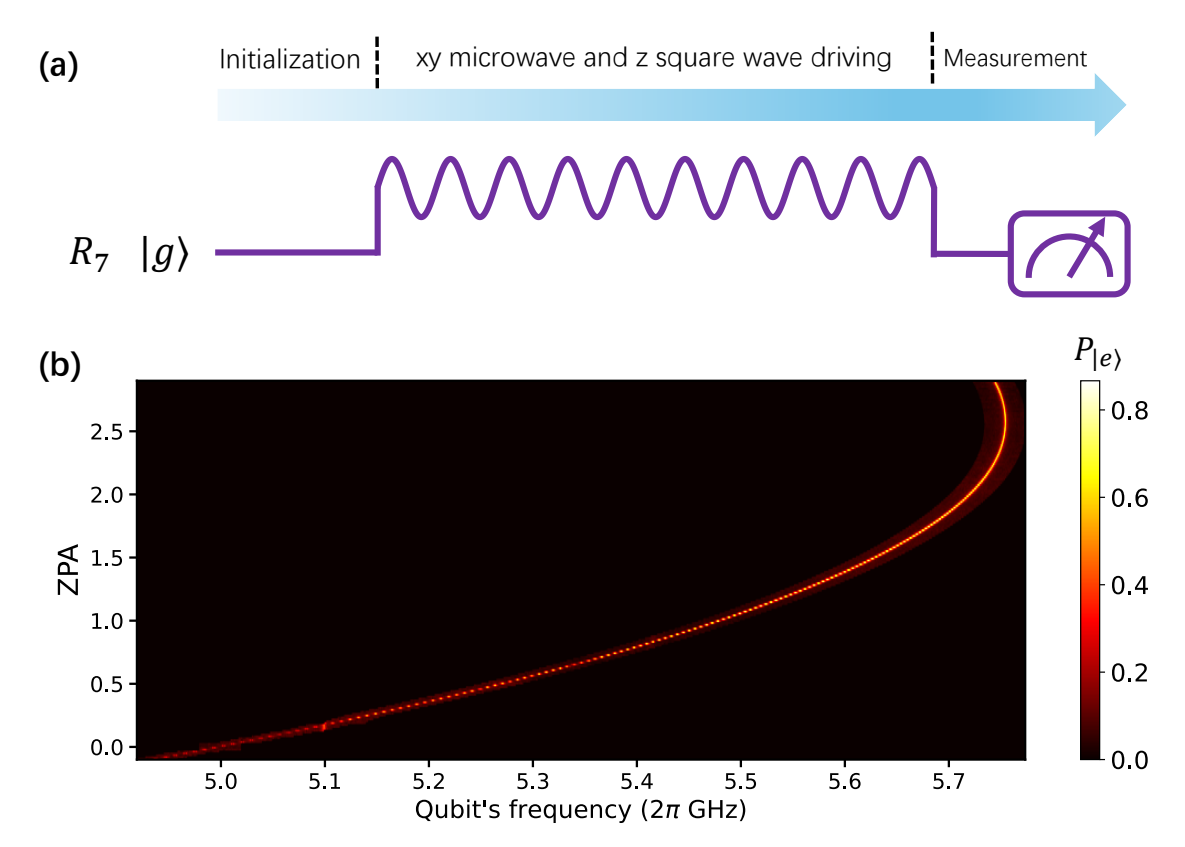


FIG. S3. Mapping between ZPA and the qubit frequency. (a) Pulse sequence: initialization in $|g\rangle$, concurrent XY-line microwave tone and Z-line square wave, followed by measurement. The ZPA sets the qubit frequency; the XY tone probes resonance. (b) Excited-state population versus XY-drive frequency and ZPA; the bright resonance ridge yields $f_q(\text{ZPA})$. The same protocol is applied to all qubits to obtain per-qubit calibrations.

B. Verification of Z-Pulse Square-Wave Integrity

We verify the time-domain integrity of the Z square pulse by fixing the XY-line microwave at a constant amplitude [on-resonance Rabi rate $\Omega^Z/(2\pi)\approx 3~\mathrm{MHz}$] and a fixed drive frequency $\omega_d^Z/(2\pi)=5.6~\mathrm{GHz}$. For each ZPA, the Z-line square wave shifts the qubit's angular frequency ω_q^Z , thereby yielding a detuning in the drive frame

$$\delta^{Z}(t) = \omega_{q}^{Z}(t) - \omega_{d}^{Z},\tag{S23}$$

where the superscript Z denotes quantities defined for this Z-pulse verification (the ZPA dependence is implicit below). The pulse sequence is analogous to the mapping sequence of Fig. S3(a): initialize the qubit in $|g\rangle$, apply a concurrent XY-line microwave tone (fixed amplitude and frequency) and a Z-line square wave, and then measure the qubit state as a function of the evolution time t. Panel (b) records the resulting Rabi-oscillation traces versus time for different ZPA values, and panel (c) shows their Fourier spectra taken along the time axis.

In the rotating frame, the driven two-level Hamiltonian is

$$H(t) = \frac{1}{2} \delta^{Z}(t) \sigma_{z} + \frac{1}{2} \Omega^{Z} \sigma_{x}, \tag{S24}$$

with the generalized Rabi frequency

$$\Omega_R^Z(t) = \sqrt{(\Omega^Z)^2 + \left[\delta^Z(t)\right]^2}.$$
 (S25)

Starting from $|g\rangle$, the excited-state probability reads

$$P_{|e\rangle}(t) \approx \frac{(\Omega^Z)^2}{\left[\Omega_R^Z(t)\right]^2} \sin^2\left(\frac{1}{2}\Omega_R^Z(t)\,t\right).$$
 (S26)

Hence the oscillation frequency along the time axis equals $\Omega_R^Z(t)/(2\pi)$: it is minimal at zero detuning $(\delta^Z=0)$ and increases monotonically with $|\delta^Z|$. For each ZPA we Fourier-transform the time traces to obtain Fig. S4(c); the V-shaped spectral ridge follows $\Omega_R^Z/(2\pi)$ with its minimum at $\Omega^Z/2\pi\approx 3$ MHz when $\delta^Z=0$. By locating, for each time slice, the ZPA where this spectral peak is minimal, we obtain the locus $\delta^Z(t)=0$, which vertically outlines how the Z pulse sets the qubit frequency throughout the pulse. An ideal square wave yields a flat (vertical) trace; any tilt or curvature indicates distortion (e.g., capacitive filtering). We use this diagnostic to predistort the Z waveform (e.g., exponential or Gaussian edge compensation) until the zero-detuning trace is flat. The same verification-and-correction procedure is applied to all qubits.

C. Calibration of Qubit Z-Line Crosstalk

Because the Z lines are routed in close proximity, driving one qubit can induce a smaller square-wave component on another. When a Z square wave with amplitude Z_1 is applied to A_1 , a parasitic input appears on the Z line of A_2 . To cancel it, we apply a compensation square wave with amplitude Z_2 on A_2 , while simultaneously driving A_2 on its XY line at the idle frequency. By scanning Z_1 and Z_2 and measuring the excited-state population of A_2 , we obtain a two-dimensional map [Fig. S5(b)] whose bright ridge yields the linear relation

$$Z_2 = \alpha_{21}^Z Z_1, (S27)$$

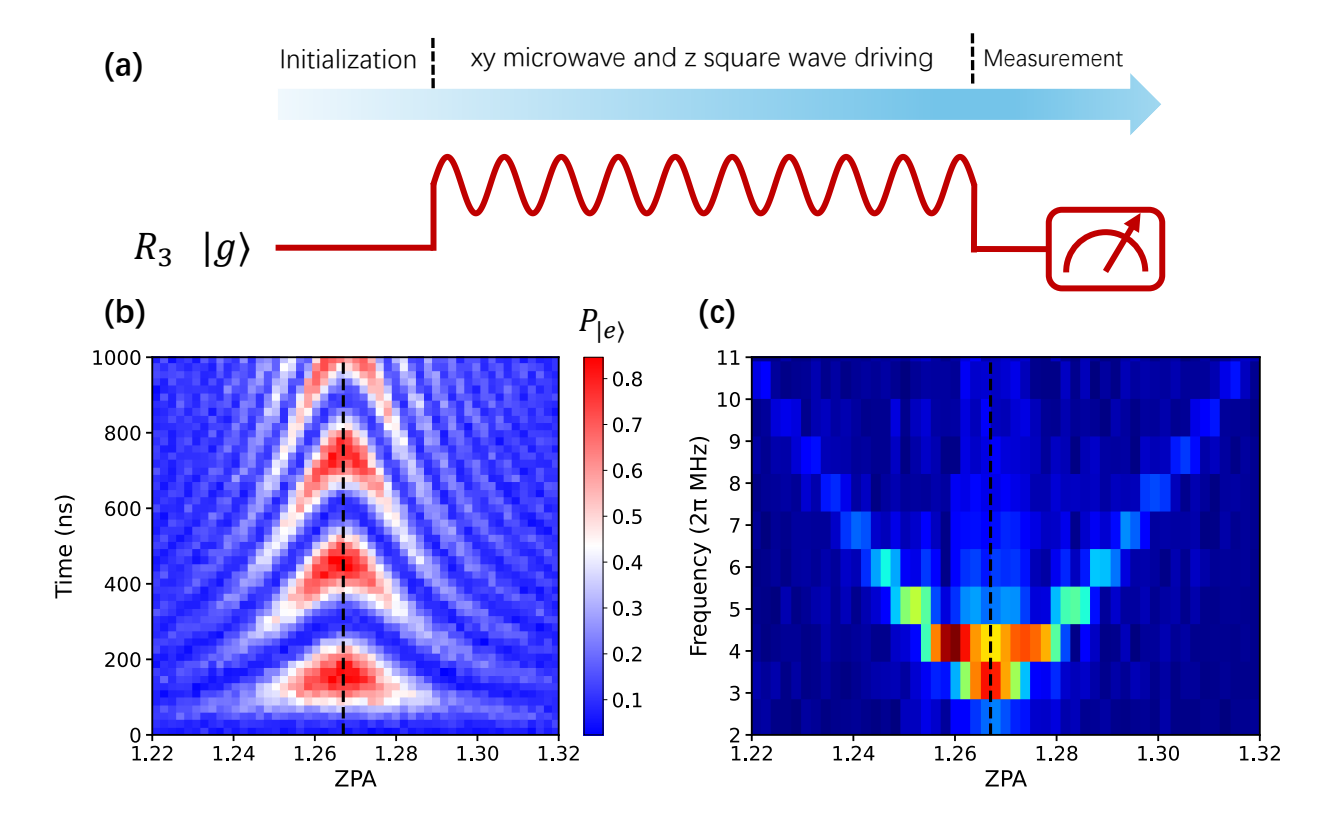


FIG. S4. Verification of Z-pulse square-wave integrity. (a) Pulse sequence for the verification, analogous to the ZPA—frequency mapping in Fig. S3(a): initialization in $|g\rangle$, concurrent XY-line microwave tone (fixed amplitude and frequency) and Z-line square wave, followed by measurement. (b) Rabi-oscillation traces versus time for different ZPA values; the dashed line marks the ZPA at which $\delta^Z=0$ for selected times. (c) Fourier spectrum (computed along t) versus ZPA. The V-shaped ridge follows $\Omega^Z_R/(2\pi)$ [Eq. (S25)], minimizing at $\Omega^Z/2\pi$ when $\delta^Z=0$. The time-dependent locus of minimal frequency reveals the temporal shape imparted by the Z pulse and is used to predistort the waveform to an ideal square.

where α_{21}^Z quantifies the Z crosstalk from $A_1 \to A_2$. In subsequent experiments, for any commanded Z_1 we set Z_2 according to Eq. (S27) so that the frequency of A_2 remains fixed.

Ramsey verification. We further verify the calibration with a Ramsey interferometry on A_2 . Two $\pi/2$ pulses on the XY line of A_2 , separated by a variable delay, are applied while the Z square waves are present. The XY carrier is detuned from the idle frequency by a preset value

$$f_R^{\text{base}} = 5 \text{ MHz},$$
 (S28)

so that in the absence of crosstalk the Ramsey fringes oscillate at f_R^{base} . If the Z pulse on A_1 shifts the frequency of A_2 by δ_{21}^Z , the observed Ramsey frequency becomes

$$f_R = f_R^{\text{base}} + \delta_{21}^Z. \tag{S29}$$

We compare three cases: (i) $Z_1=0$ (baseline), yielding $f_R=f_R^{\rm base}$; (ii) $Z_1=1$ without compensation, giving a shifted frequency $f_R^{\rm ct}\neq f_R^{\rm base}$; (iii) $Z_1=1$ with compensation $Z_2=\alpha_{21}^ZZ_1$, which restores the Ramsey frequency to $f_R^{\rm base}$. The recovery of the 5-MHz fringes demonstrates that the Z crosstalk has been effectively canceled. This protocol can be repeated for any pair of qubits to obtain the full set of crosstalk coefficients α_{ij}^Z .

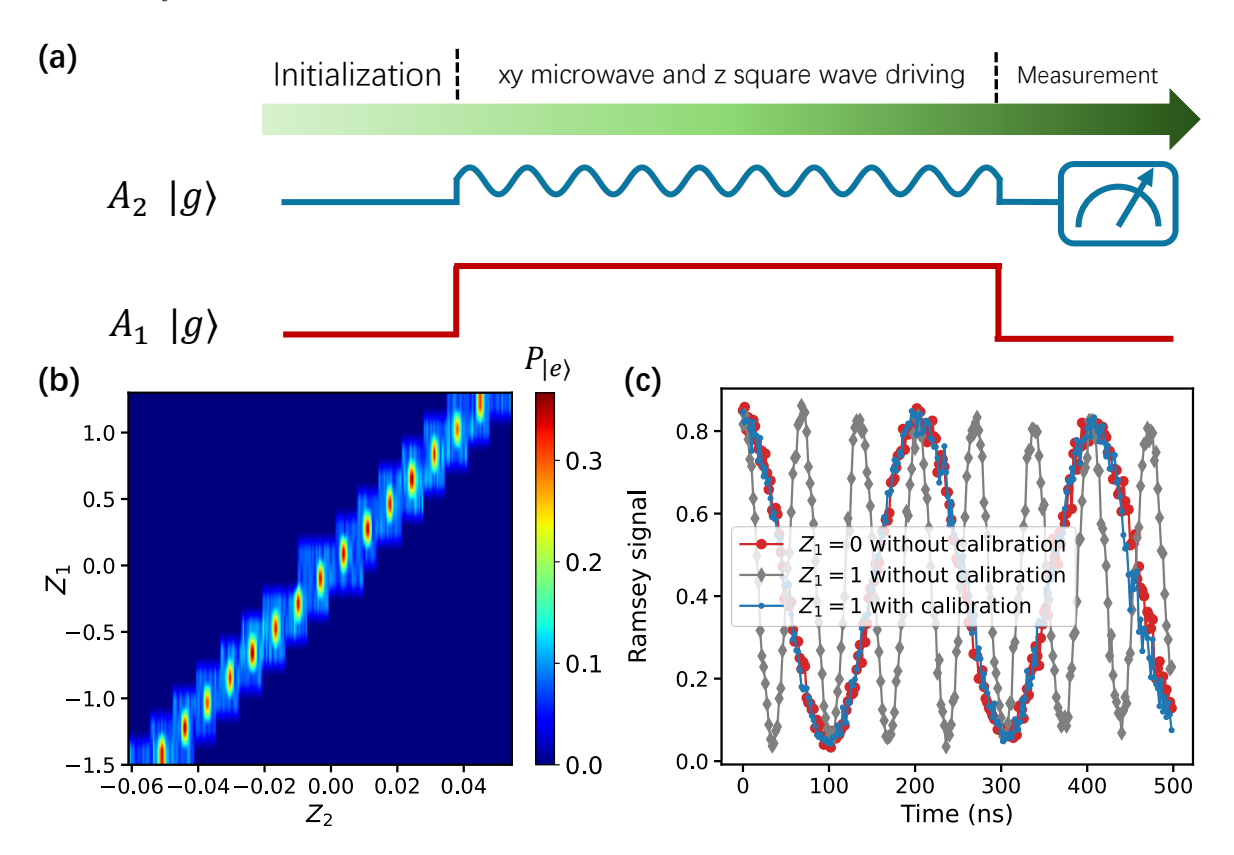


FIG. S5. Calibration of the Z crosstalk. (a) Pulse sequence. Apply a Z-line square wave of amplitude Z_1 to A_1 and, simultaneously, a small Z square wave of amplitude Z_2 to A_2 ; keep an XY-line microwave on A_2 at its idle frequency; then measure A_2 . (b) Excited-state population of A_2 versus Z_1 and Z_2 . The bright ridge gives $Z_2 = \alpha_{21}^Z Z_1$. (c) Ramsey verification on A_2 with preset baseline $f_R^{\text{base}} = 5$ MHz: comparison among $Z_1 = 0$ (baseline), $Z_1 = 1$ without compensation (frequency shifted), and $Z_1 = 1$ with compensation $Z_2 = \alpha_{21}^Z Z_1$ (frequency restored).

Once the pairwise coefficients α_{ij}^Z are measured, we arrange the Z amplitudes as column vectors

$$\mathbf{Z}^{\text{cmd}} = \begin{bmatrix} Z_1^{\text{cmd}} \\ Z_2^{\text{cmd}} \\ \vdots \\ Z_N^{\text{cmd}} \end{bmatrix}, \qquad \mathbf{Z}^{\text{eff}} = \begin{bmatrix} Z_1^{\text{eff}} \\ Z_2^{\text{eff}} \\ \vdots \\ Z_N^{\text{eff}} \end{bmatrix}, \tag{S30}$$

where Z_j^{cmd} is the commanded square-wave amplitude put on the physical Z line of qubit j, and Z_i^{eff} is the

amplitude effectively experienced by qubit i after crosstalk.

The two are connected by the correction matrix M_{cor} ,

$$\mathbf{Z}^{\text{eff}} = M_{\text{cor}} \mathbf{Z}^{\text{cmd}}, \tag{S31}$$

whose explicit form (for N qubits) is

$$M_{\text{cor}} = \begin{bmatrix} 1 & -\alpha_{12}^{Z} & -\alpha_{13}^{Z} & \cdots & -\alpha_{1N}^{Z} \\ -\alpha_{21}^{Z} & 1 & -\alpha_{23}^{Z} & \cdots & -\alpha_{2N}^{Z} \\ -\alpha_{31}^{Z} & -\alpha_{32}^{Z} & 1 & \cdots & -\alpha_{3N}^{Z} \\ \vdots & \vdots & \vdots & \ddots & \vdots \\ -\alpha_{N1}^{Z} & -\alpha_{N2}^{Z} & -\alpha_{N3}^{Z} & \cdots & 1 \end{bmatrix},$$
(S32)

with diagonal entries 1 (local action) and off-diagonal entries $-\alpha_{ij}^Z$ [parasitic contribution from j to i, extracted from the compensation ridge in Fig. S5(b)].

Given a desired effective configuration $\mathbf{Z}_*^{\mathrm{eff}}$, the commanded amplitudes are obtained by solving the linear system

$$M_{\text{cor}} \mathbf{Z}^{\text{cmd}} = \mathbf{Z}_{*}^{\text{eff}} \quad \Rightarrow \quad \mathbf{Z}^{\text{cmd}} = M_{\text{cor}}^{-1} \mathbf{Z}_{*}^{\text{eff}}.$$
 (S33)

Operationally, once $M_{\rm cor}$ is calibrated, each programmed Z waveform is pre-multiplied by $M_{\rm cor}^{-1}$ before being sent to the hardware, so that the qubits receive the intended effective Z amplitudes during experiments.

S4. SIDEBAND COUPLING VIA FLOQUET MODULATION

We consider a Xmon qubit R_j dispersively coupled to a cavity mode. The cavity annihilation (creation) operator is a (a^{\dagger}) with angular frequency ω_s . The symbol q (q^{\dagger}) denotes the annihilation (creation) operator of the anharmonic oscillator mode of qubit R_j , whose mean angular frequency is ω_j^m . In what follows, we assume $\delta_j = 0$ for all R_j .

To realize the first-order sideband, we set the qubit angular frequency to

$$\omega_j^m = \omega_s - \nu_j. \tag{S34}$$

A sinusoidal frequency modulation is applied to the qubit frequency. The total Hamiltonian is $(\hbar = 1)$

$$H = H_0 + H_I, \tag{S35}$$

$$H_0 = \omega_s a^{\dagger} a + \left[\omega_j^m + \varepsilon_j \cos(\nu_j t)\right] q^{\dagger} q - \frac{K_j}{2} q^{\dagger 2} q^2, \tag{S36}$$

$$H_I = \xi_j \, a^{\dagger} q + \text{h.c.} \,. \tag{S37}$$

Here ε_j and ν_j are the amplitude and angular frequency of the qubit-frequency modulation, ξ_j is the coupling strength between R_j and the cavity, and K_j is the anharmonicity of R_j .

We keep the lowest three levels $\{|g\rangle, |e\rangle, |f\rangle\}$ of R_j and move to the rotating frame of H_0 with

$$U_0(t) = \exp\left\{i\left[\omega_s a^{\dagger} a + \left(\omega_j^m + \varepsilon_j \cos(\nu_j t)\right) |e\rangle\langle e| + (2\omega_j^m - K_j)|f\rangle\langle f|\right]t\right\}.$$
 (S38)

Defining the modulation index $\mu_j=arepsilon_j/
u_j$, the interaction in this frame is

$$H_I' = \left\{ e^{-i\mu_j \sin(\nu_j t)} \, \xi_j \, a^{\dagger} \left[e^{i\nu_j t} \, |g\rangle\!\langle e| + \sqrt{2} \, e^{i(\nu_j + K_j)t} \, |e\rangle\!\langle f| \right] + \text{h.c.} \right\}. \tag{S39}$$

Using the Jacobi-Anger identity,

$$e^{-i\mu_j \sin(\nu_j t)} = \sum_{n=-\infty}^{\infty} J_n(\mu_j) e^{-in\nu_j t}, \tag{S40}$$

Eq. (S39) becomes

$$H_I' = \sum_{n=-\infty}^{\infty} J_n(\mu_j) \, \xi_j \, a^{\dagger} \left[e^{-i(n-1)\nu_j t} |g\rangle\!\langle e| + \sqrt{2} \, e^{-i(n-1)\nu_j t + iK_j t} |e\rangle\!\langle f| \right] + \text{h.c.}$$
 (S41)

The factor $(n-1)\nu_j$ shows that the n=1 Floquet harmonic is stationary, which realizes the first-order sideband.

Assuming $\{|J_0(\mu_j)\xi_j|\} \ll \nu_j$ and working close to the n=1 sideband resonance, we keep the slowly varying n=1 term in the $|g\rangle\langle e|$ channel and treat the other harmonics dispersively to second order. The effective Hamiltonian is

$$H_{\text{eff}} = \left[J_1(\mu_j) \, \xi_j \, a^{\dagger} |g\rangle\langle e| + \text{h.c.} \right] + S_1 \left(|g\rangle\langle g| - |e\rangle\langle e| \right) a^{\dagger} a - S_1 \, |e\rangle\langle e| + S_2 \, |e\rangle\langle e| \, a^{\dagger} a. \tag{S42}$$

The Stark shifts induced by off-resonant harmonics $n \neq 1$ are

$$S_1 = \sum_{n \neq 1} \frac{\left[J_n(\mu_j)\,\xi_j\right]^2}{(1-n)\,\nu_j}, \qquad S_2 = \sum_{n \neq 1} \frac{2\left[J_n(\mu_j)\,\xi_j\right]^2}{(1-n)\,\nu_j + K_j}.$$
 (S43)

Therefore the first-order sideband coupling strength is

$$\frac{\lambda_j}{2} = J_1(\mu_j)\,\xi_j. \tag{S44}$$

A. Experimental demonstration of sideband coupling

To verify the sideband coupling via Floquet modulation, we perform an experiment using a single qubit R_1 coupled to a cavity. The experimental setup and results are summarized in Fig. S6. After initialization, a microwave π -pulse excites qubit R_1 from $|g\rangle$ to $|e\rangle$, preparing the joint state $|e0\rangle = |e\rangle \otimes |0\rangle_{\text{cav}}$, where the

Parameters	R_1	R_2	R_3	R_4	R_5	R_6	R_7	R_8
$ u_j/(2\pi)$ (MHz)	190	200	170	180	220	210	130	160
$\lambda_j/2~(2\pi~{ m MHz})$	4.1	3.3	2.2	2.6	2.7	2.5	2.0	3.2
$\varepsilon_j~(2\pi~{ m MHz})$	81.5	67.3	47.3	46.7	62.4	51.6	40.9	64.1
$\delta_j \ (2\pi \ \mathrm{MHz})$	0	0	0	0	0	0	0	0

TABLE S3. Floquet sideband parameters for qubits R_1 - R_8 . Each entry lists the modulation frequency $\nu_j/(2\pi)$ used for the first-order sideband, the effective coupling $\lambda_j/2$ extracted from swap oscillations $|e0\rangle \leftrightarrow |g1\rangle$ as in Fig. S6(c), the modulation amplitude ε_j , and the small detuning δ_j .

trailing numeral denotes the cavity Fock state (0 for vacuum, 1 for one photon). A Floquet Z-modulation with frequency $\nu_1/(2\pi)=190\,\mathrm{MHz}$ and amplitude $\varepsilon_1=2\pi\times81.5\,\mathrm{MHz}$ is then applied, and we measure the qubit ground-state probability P_g . Under this drive the system exhibits coherent exchange $|e0\rangle\leftrightarrow|g1\rangle$, i.e., between the qubit excitation and a single cavity photon.

Figure S6(b) shows P_g versus the detuning Δ_1 and pulse duration; the interference fringes reveal the sideband dynamics. From this map we identify the optimal detuning as $\Delta_1^{\rm opt}=2\pi\times296\,{\rm MHz}$. The calibration of qubit frequency versus ZPA is performed under square-wave pulses; in the Floquet configuration this mapping is nonlinearly distorted, shifting the apparent optimum. In our device the qubit idle frequency is $\omega_i/(2\pi)=5.3\,{\rm GHz}$ and the cavity frequency is $\omega_s/(2\pi)=5.796\,{\rm GHz}$. For the first-order sideband, the ideal detuning predicted by the model is $\Delta_{\rm ideal}=\omega_s-\omega_i-\nu_1=2\pi\times306\,{\rm MHz}$, which is slightly larger than the experimental $\Delta_1^{\rm opt}$, consistent with the nonlinear ZPA mapping.

At $\Delta_1 = \Delta_1^{\rm opt}$, P_g versus Floquet pulse length [Fig. S6(c)] oscillates with frequency $f_{\rm swap} = 8.1\,{\rm MHz}$, demonstrating coherent exchange $|e0\rangle \leftrightarrow |g1\rangle$; this corresponds to an effective sideband coupling $\lambda_1/2 = 2\pi \times 4.1\,{\rm MHz}$. These observations quantitatively confirm the realization of sideband coupling via Floquet modulation in our system.

To benchmark the Floquet sideband across the full register, we extract for each qubit R_j (j = 1, ..., 8) the Floquet modulation frequency $\nu_j/(2\pi)$, the effective coupling $\lambda_j/2$, the modulation amplitude ε_j , and the small detuning δ_j from datasets analogous to Figs. S6(b,c). The summary is organized in Table S3.

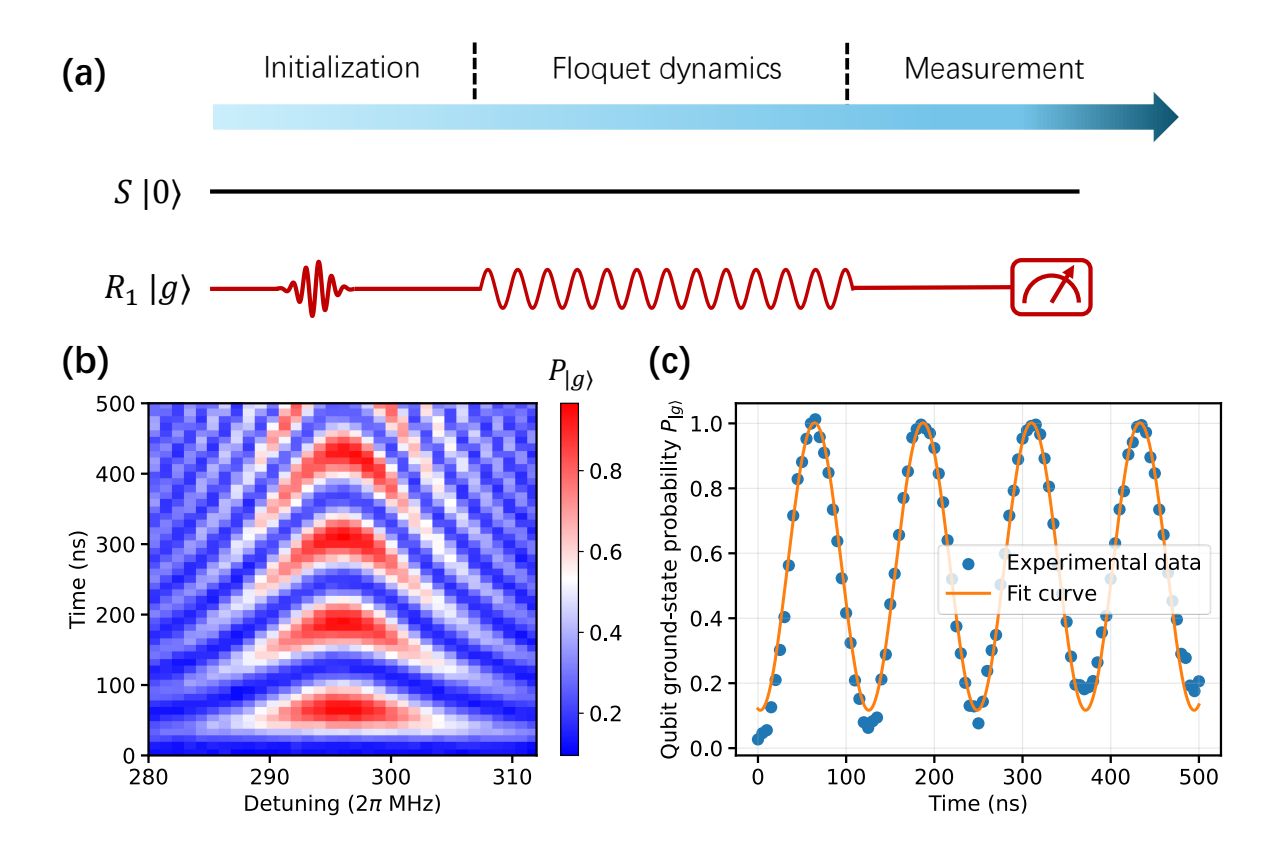


FIG. S6. Experimental demonstration of sideband coupling via Floquet modulation. (a) Pulse sequence: a microwave π -pulse prepares the joint state $|e0\rangle$ (qubit in $|e\rangle$, cavity in vacuum $|0\rangle_{\rm cav}$), followed by a Floquet Z-modulation and measurement. (b) Qubit ground-state probability P_g versus detuning Δ_1 and pulse duration under a Floquet pulse with $\nu_1/(2\pi)=190\,{\rm MHz}$ and $\varepsilon_1=2\pi\times81.5\,{\rm MHz}$; the optimal operating point occurs near $\Delta_1^{\rm opt}=2\pi\times296\,{\rm MHz}$. (c) P_g versus pulse duration at $\Delta_1^{\rm opt}$, showing coherent exchange $|e0\rangle\leftrightarrow|g1\rangle$. A sinusoidal fit yields $f_{\rm swap}=8.1\,{\rm MHz}$, implying an effective coupling $\lambda_1/2=2\pi\times4.1\,{\rm MHz}$.

S5. PHOTON NUMBER DISTRIBUTION MEASUREMENT AND WIGNER TOMOGRAPHY

A. Photon-number readout via a resonant ancilla qubit

We use the ancilla qubit A_1 to read out the photon-number distribution of the bus resonator B. After a given dynamical evolution, the resonator reaches a state ρ_S . Figure S7(a) illustrates the measurement sequence: A_1 is initialized in $|g\rangle$, while the resonator is in ρ_S . After turning off all drives, the frequency of A_1 is tuned on resonance with B for a variable interaction time τ , after which the qubit is parked back to its idle point and measured.

The dynamics are governed by the resonant Jaynes-Cummings Hamiltonian

$$H = \omega_s a^{\dagger} a + \frac{\omega_s}{2} \sigma_z + \xi \left(a \sigma_+ + a^{\dagger} \sigma_- \right), \tag{S45}$$

where a is the annihilation operator of B, σ_{\pm} act on $\{|g\rangle, |e\rangle\}$ of A_1 , and ξ is the coupling strength. In each Fock subspace $\{|g,n\rangle, |e,n-1\rangle\}$ $(n \geq 1)$, the system undergoes Rabi oscillations at frequency $2\xi\sqrt{n}$, while the vacuum $|g,0\rangle$ does not oscillate.

Let $P_n = \langle n | \rho_S | n \rangle$ denote the photon-number distribution of the resonator. The excited-state probability of A_1 is then described by [S2, S3]

$$P_e(\tau) = \frac{1}{2} \left\{ 1 - \left[P_{|g\rangle}(0) - P_{|e\rangle}(0) \right] \sum_{n=0}^{n_{\text{max}}} P_n \cos(2\xi \sqrt{n} \,\tau) \right\}.$$
 (S46)

Here $P_{|g\rangle}(0)$ and $P_{|e\rangle}(0)$ denote the initial ground- and excited-state populations of A_1 . In principle $P_{|e\rangle}(0) = 0$, but in practice a small residual excitation is observed due to the finite detuning (~ 700 MHz) between the idle qubit frequency and the resonator when many photons are present. This offset causes the oscillations to center around the actual experimental mean excitation probability rather than exactly 1/2.

The photon-number distribution $\{P_n\}$ is obtained by fitting the measured $P_e(\tau)$ to Eq. (S46). In practice, we perform a least-squares fit, where the free parameters are the probabilities $\{P_n\}$ constrained to satisfy $P_n \geq 0$ and $\sum_n P_n = 1$. An example of the measured Rabi signal and the extracted distribution is shown in Figs. S7(b,c).

B. Wigner tomography

To reconstruct the resonator state in phase space, we apply a displacement operator

$$D(\alpha) = \exp(\alpha a^{\dagger} - \alpha^* a), \tag{S47}$$

realized by a calibrated resonator drive whose amplitude and phase define α . The displaced state is

$$\tilde{\rho}_S(\alpha) = D^{\dagger}(\alpha) \,\rho_S \,D(\alpha). \tag{S48}$$

The photon-number probabilities of the displaced state are

$$\tilde{P}_n(\alpha) = \langle n | \, \tilde{\rho}_S(\alpha) \, | n \rangle \,. \tag{S49}$$

The Wigner function is then obtained from the parity relation

$$W(\alpha) = \frac{2}{\pi} \sum_{n=0}^{\infty} (-1)^n \tilde{P}_n(\alpha).$$
 (S50)

For convenience, we parameterize α in terms of the canonical quadratures

$$x = \frac{\alpha + \alpha^*}{\sqrt{2}}, \qquad p = \frac{\alpha - \alpha^*}{i\sqrt{2}},$$
 (S51)

so that $\alpha = (x + ip)/\sqrt{2}$. By scanning $\operatorname{Re} \alpha$ and $\operatorname{Im} \alpha$ over a two-dimensional grid, we reconstruct $W(\operatorname{Re} \alpha, \operatorname{Im} \alpha)$ of the state ρ_S , as shown in the main text.

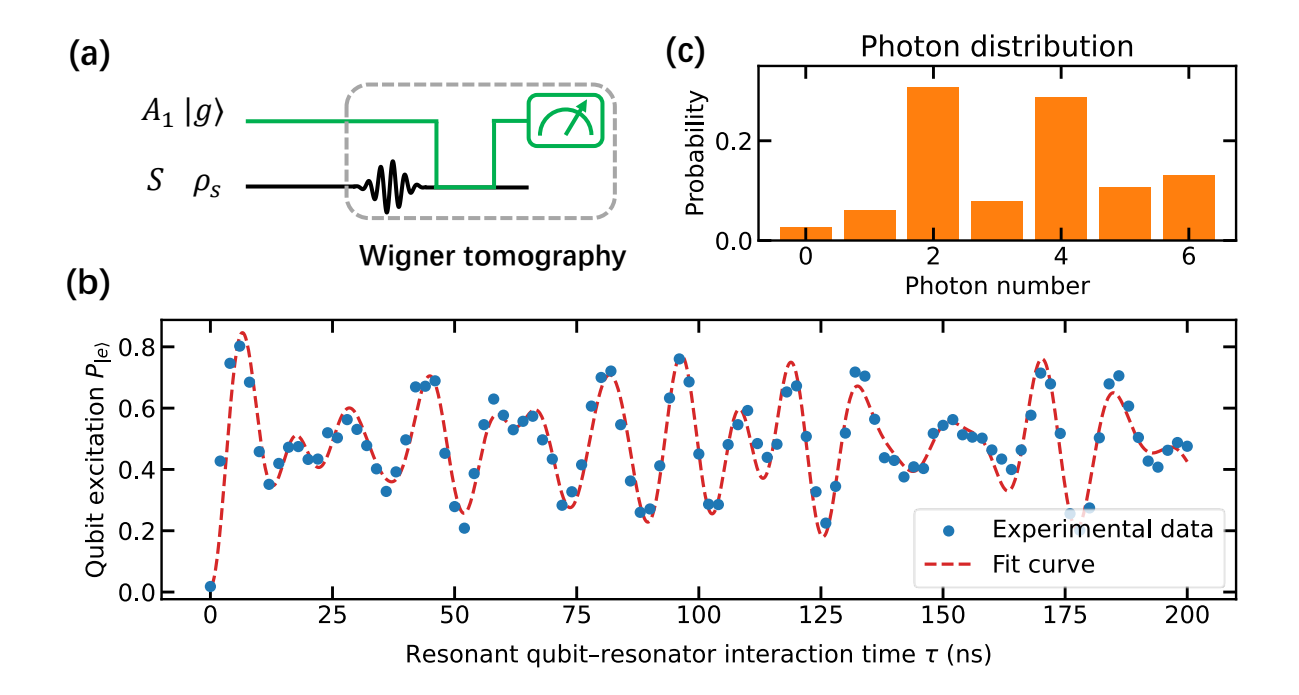


FIG. S7. Photon-number readout and Wigner tomography. (a) Measurement sequence. The ancilla qubit A_1 is initialized in $|g\rangle$, while the bus resonator B is in a state ρ_S observed after dynamical evolution. After turning off all drives, A_1 is tuned on resonance with B for a variable interaction time τ , then parked back to its idle frequency and measured. (b) Measured excited-state probability $P_e(\tau)$ of A_1 (blue dots) as a function of the resonant interaction time τ . The red dashed curve is a least-squares fit to Eq. (S46), where the oscillation frequencies $2\xi\sqrt{n}$ reflect contributions from different photon numbers. (c) Photon-number distribution $\{P_n\}$ extracted from (b). The resonator state here is ρ_S without any prior displacement $D(\alpha)$, i.e., $\alpha=0$. This example illustrates the case of a low-photon-number state.

S6. DERIVATION AND CALCULATION OF DISTINGUISHABILITY

A. Definition

The distinguishability \mathcal{D} quantifies the degree to which the reservoir states corresponding to different field branches can be distinguished. It is defined as the trace distance

$$\mathcal{D} = \frac{1}{2} \operatorname{Tr} \left| \rho^{|0\rangle} - \rho^{|\alpha\rangle} \right|, \tag{S52}$$

where $\rho^{|0\rangle}$ and $\rho^{|\alpha\rangle}$ are the reduced reservoir states conditioned on the vacuum and coherent components of the field, respectively. The notation $|\cdot|$ indicates the positive semidefinite operator obtained by taking absolute values of the eigenvalues, i.e.,

$$\mathcal{D} = \frac{1}{2} \sum_{i} |\lambda_i| \tag{S53}$$

with $\{\lambda_i\}$ the eigenvalues of $\Delta = \rho^{|0\rangle} - \rho^{|\alpha\rangle}$.

B. Distinguishability and many-qubit reservoir

After the system–reservoir interaction, the joint state is well approximated by

$$|\psi(t)\rangle \simeq \frac{1}{\sqrt{2}} \Big(|0\rangle \otimes |\phi^{|0\rangle}\rangle + |\alpha\rangle \otimes |\phi^{|\alpha\rangle}\rangle \Big),$$
 (S54)

with

$$|\phi^{|0\rangle}\rangle = \bigotimes_{k=1}^{N} |g\rangle_k, \qquad |\phi^{|\alpha\rangle}\rangle = \bigotimes_{k=1}^{N} \left(c_k^g |g\rangle_k + c_k^e |e\rangle_k\right),$$
 (S55)

where the single-qubit amplitudes are given by

$$c_k^g(t) = \cos\left(\frac{\Omega_k t}{2}\right) + i\frac{\delta_k}{\Omega_k}\sin\left(\frac{\Omega_k t}{2}\right),$$
 (S56a)

$$c_k^e(t) = -i \frac{\sqrt{\langle n \rangle} \lambda_k}{\Omega_k} \sin\left(\frac{\Omega_k t}{2}\right),$$
 (S56b)

$$\Omega_k = \sqrt{\langle n \rangle \, \lambda_k^2 + \delta_k^2} \,. \tag{S56c}$$

Projecting onto the field branches and tracing out the field gives the two branch-conditioned reservoir states

$$\rho^{|0\rangle} = |\phi^{|0\rangle}\rangle\langle\phi^{|0\rangle}|, \qquad \rho^{|\alpha\rangle} = |\phi^{|\alpha\rangle}\rangle\langle\phi^{|\alpha\rangle}|. \tag{S57}$$

In experiments we reconstruct the unconditional reduced state of the reservoir,

$$\rho^{R} = \text{Tr}_{S}(|\psi(t)\rangle\langle\psi(t)|) \simeq \frac{1}{2}|\phi^{|0\rangle}\rangle\langle\phi^{|0\rangle}| + \frac{1}{2}|\phi^{|\alpha\rangle}\rangle\langle\phi^{|\alpha\rangle}| + \mathcal{O}(\langle 0|\alpha\rangle), \tag{S58}$$

where the small cross terms proportional to $\langle 0|\alpha\rangle=e^{-|\alpha|^2/2}$ have been neglected. Taking the partial trace over all qubits except k yields

$$\rho_k \simeq \frac{1}{2} |g\rangle_k \langle g| + \frac{1}{2} \rho_k^{|\alpha\rangle},\tag{S59}$$

where the branch-conditioned state of the kth qubit is

$$\rho_k^{|\alpha\rangle} = |\phi_k\rangle\langle\phi_k|, \qquad |\phi_k\rangle = c_k^g |g\rangle_k + c_k^e |e\rangle_k. \tag{S60}$$

In practice, from tomography one extracts ρ_k and obtains the normalized form of $\rho_k^{|\alpha\rangle}$ as

$$\rho_k^{|\alpha\rangle} \simeq 2\rho_k - |q\rangle_k \langle q|.$$
(S61)

So when the backaction-induced inter-qubit correlations in the $|\alpha\rangle$ branch are weak, the conditioned reservoir state factorizes to leading order,

$$\rho^{|\alpha\rangle} \simeq \bigotimes_{k=1}^{N} \rho_k^{|\alpha\rangle}, \qquad \rho^{|0\rangle} = \bigotimes_{k=1}^{N} |g\rangle_k \langle g|.$$
(S62)

C. Ensuring Positive Semidefinite Reconstruction

The approximate single-qubit branch state obtained from tomography,

$$\rho_k^{|\alpha\rangle} \simeq 2 \,\rho_k - |g\rangle_k \,\langle g| \,,$$
(S63)

provides a convenient linear estimate. However, the linear relation in Eq. (S63) does not, in general, preserve positive semidefiniteness, even in the absence of experimental noise. To restore physicality, $\rho_k^{|\alpha\rangle}$ is projected onto the set of unit-trace positive semidefinite matrices via eigenvalue decomposition.

We first compute its spectral decomposition,

$$\rho_k^{|\alpha\rangle} = V \operatorname{diag}(\lambda_1, \dots, \lambda_d) V^{\dagger}, \tag{S64}$$

and then remove any negative eigenvalues,

$$\lambda_i' = \max(\lambda_i, 0) \qquad (i = 1, \dots, d). \tag{S65}$$

The matrix is subsequently normalized to restore unit trace,

$$\tilde{\rho}_k^{|\alpha\rangle} = V \operatorname{diag}\left(\frac{\lambda_1'}{\sum_j \lambda_j'}, \dots, \frac{\lambda_d'}{\sum_j \lambda_j'}\right) V^{\dagger}. \tag{S66}$$

The resulting matrix satisfies

$$\tilde{
ho}_k^{|lpha
angle}$$
 is positive semidefinite, ${
m Tr}[\tilde{
ho}_k^{|lpha
angle}]=1,$ (S67)

and coincides with Eq. (S63) whenever the latter is already positive semidefinite and normalized.

Applying this procedure qubit by qubit ensures that all reconstructed branch states are physical, and that the factorized reservoir state

$$\rho^{|\alpha\rangle} \simeq \bigotimes_{k=1}^{N} \tilde{\rho}_{k}^{|\alpha\rangle} \tag{S68}$$

remains a valid positive semidefinite density operator for further analysis.

^{*} xia-208@163.com

[†] zbyang@fzu.edu.cn

[‡] t96034@fzu.edu.cn

[[]S1] C. K. Law and J. H. Eberly, Arbitrary control of a quantum electromagnetic field, Phys. Rev. Lett. **76**, 1055 (1996).

- [S2] M. Hofheinz, H. Wang, M. Ansmann, R. C. Bialczak, E. Lucero, M. Neeley, A. D. O'Connell, D. Sank, J. Wenner, J. M. Martinis, and A. N. Cleland, Synthesizing arbitrary quantum states in a superconducting resonator, Nature 459, 546 (2009).
- [S3] R.-H. Zheng, W. Ning, Y.-H. Chen, J.-H. Lü, L.-T. Shen, K. Xu, Y.-R. Zhang, D. Xu, H. Li, Y. Xia, F. Wu, Z.-B. Yang, A. Miranowicz, N. Lambert, D. Zheng, H. Fan, F. Nori, and S.-B. Zheng, Observation of a superradiant phase transition with emergent cat states, Phys. Rev. Lett. **131**, 113601 (2023).